

Photometric White Dwarf Rotation

1 GABRIELA OLIVEIRA DA ROSA,¹ S. O. KEPLER,¹ L. T. T. SOETHE,^{2,1} ALEJANDRA D. ROMERO,¹ AND KEATON J. BELL³

2 ¹*Instituto de Física, Universidade Federal do Rio Grande do Sul*
3 *91501-970 Porto Alegre, RS, Brazil*

4 ²*Instituto Federal de Educação, Ciência e Tecnologia Sul-rio-grandense*
5 *96745-000 Charqueadas, RS, Brazil*

6 ³*Department of Physics, Queens College, City University of New York,*
7 *Flushing, NY, 11367, USA*

ABSTRACT

8
9 We present a census of photometrically detected rotation periods for white dwarf stars. We analyzed
10 the 9285 White Dwarfs observed by *TESS* telescope up to sector 69. We inspected the 21 832 light
11 curves obtained for these stars using Fourier transform analyses and the *TESS-Localize* software to
12 confirm the origin of the detected signals. As a result, we determined the rotation periods for 267 white
13 dwarf stars, excluding pulsations and linear combinations. More than 60% of the stars composing our
14 sample present rotation period shorter than 10 *h*. Consequently, the median rotation period of our
15 sample is 7.3 *h*, way shorter than the median period reported by previous work. For the stars in binary
16 systems, we do not observe a preferential mass, temperature, or period. On the other hand, we observe
17 that magnetic stars tend to present a higher mass, lower temperature, and shorter periods. Compiling
18 all the rotation periods estimated through asteroseismology and reported until now, we found that
19 seismological rotation periods exhibit a distribution similar to the distribution of our photometrical
20 sample. In addition, we calculated evolutionary models trying to reproduce our findings. Our models
21 indicate that the temperature-period relation of most observational data is best fitted by no angular
22 momentum transport mechanism activated in models with initial rotational velocity 50 km s⁻¹ and
23 $Z = 0.02$ metallicity or by models with $Z = 0.001$ metallicity and initial rotational velocity 10 km s⁻¹.

INTRODUCTION

24
25 The rotation period is an essential parameter for the
26 study of stellar evolution. It plays a significant role in
27 the stellar dynamo mechanism and is directly related
28 to the mass loss experienced by stars during the asymp-
29 totic giant branch (AGB). For both single stars and stars
30 in binary systems, photometry allows us to detect the
31 rotation period of stars directly and indirectly through
32 asteroseismology.

33 Binary stellar systems can exhibit light variability due
34 to different effects. Depending on the geometry of the
35 system and the orientation of the orbital plane as ob-
36 served from Earth, light variability from binary systems
37 can provide the rotational period of stars or the system's
38 orbital period. Variability resulting from ellipsoidal vari-
39 ation or reflection in binary systems provides stellar ro-
40 tation periods, whereas variability from orbital motion
41 indicates the system's orbital period (e.g. [Krtićka et al.](#)
42 [2023](#)). However, in the case of spin-orbit coupling, there
43 is no difference between orbital and rotational periods.
44 The spin-orbit coupling occurs when there is mass loss
45 due to winds, trying to balance the variation in the spin

46 of each star with the angular momentum of the sys-
47 tem. [Zahn \(1977\)](#) demonstrated that the synchroniza-
48 tion time between the stellar rotation and the orbital
49 period of a binary system is proportional to P_{orb}^4 , where
50 P_{orb} is the orbital period of the system. This implies
51 that the shorter the orbital period, the faster the syn-
52 chronization process occurs. [Zahn \(1977\)](#), suggests that
53 periods smaller than 17 days are synchronized.

54 Single stars, like our Sun, may also exhibit light vari-
55 ability due to the presence of dark spots and patches on
56 their surface. hese inhomogeneities are typically associ-
57 ated with the presence of a magnetic field or chemical
58 composition variation across the stellar surface. In this
59 case, the rotation period as well as some harmonics can
60 be present in the light curves, depending on the number
61 of spots.

62 Luminosity variations due to rotation are detected in
63 white dwarf stars in single and multiple systems. White
64 dwarf (WD) stars are the most common end of stellar
65 evolution, constituting the fate of 95 – 97% of all stars
66 in the Galaxy (e.g. [García-Berro et al. 1997](#); [Poelarends](#)
67 [et al. 2008](#); [Siess 2010](#); [Langer 2012](#); [Woosley & Heger](#)

2015; Doherty et al. 2014). As fossils, WDs preserve valuable information about their past evolution, making them essential for studying our Galaxy’s structure, evolution, chemical enrichment, and star formation history (Diaz-Pinto et al. 1994). WDs are classified into spectral classes based on the dominant chemical element on their surface. Approximately 80% of all WDs belong to the DA spectral type (e.g. Kepler et al. 2021), with the spectra showing only hydrogen (H) lines. The remaining 20% mainly consists of WD stars of spectral types DB and DO, featuring helium-dominated atmospheres. DOs are characterized by spectra with high-excitation lines of He II, C IV, O VI, and N V, and T_{eff} exceeding 40,000 K.

Although WDs have been studied since 1915 (Adams 1915), their rotation period distribution is still largely undetermined. Ground-based observations cannot easily measure rotation periods because of atmospheric and instrumental limitations, as WDs are intrinsically faint stars. Furthermore, the time gap due to daylight constrains the period range that can be determined (Nather et al. 1990). The long-time-baseline observations from space-based telescopes have largely overcome the latter problem. The *Kepler* spacecraft was launched in 2009, obtaining excellent data to search for stellar variability. The failure of its second reaction wheel in 2013 led to significant noise issues at low frequencies. It presented a serious challenge in identifying rotation periods for faint stars. The launch of the *TESS* telescope in 2018 (2014) allowed a reliable analysis of low frequencies for WD stars. Even with many gaps, *TESS* data enabled the detection of photometric rotation periods directly in the frequency spectrum. Finally, the high-precision astrometry obtained by the *Gaia* mission (Gaia Collaboration et al. 2018), has improved the identification of the objects considerably and thus the photometric analysis.

Alternatively, it is also possible to estimate the stellar rotation period of stars through asteroseismology, by studying their pulsation period spectra as in Kepler & Romero (2017). For instance, Hermes et al. (2017b) estimated the rotation period for twenty WDs, all pulsating hydrogen atmosphere DAVs, using data from the *Kepler* spacecraft. The authors combined these results with the early estimates compiled by Kawaler (2015), and found a mean rotation period of 35 ± 28 h for a sample of 40 objects, with a slight tendency to shorter periods for higher masses.

This work presents the first analysis of the rotation period distribution of a large sample of WD stars based on photometric data from the *TESS* telescope. We analyzed 21 832 light curves of the 9285 white dwarfs observed by *TESS* from sectors 1 to 69. We searched for

stable variability and used the *TESS-Localize* software to confirm the signal source, as presented in Section 1. In section 2, we present the results for the rotation period distribution for 267 WDs and analyze its dependence on the stellar parameters. We also perform theoretical model computations to analyze the effects of different angular momentum transfer mechanisms present during the WD evolution (Section 3). Finally, we present our concluding remarks in Section 4.

1. DATA ANALYSIS

We selected all known WDs, including *Gaia* candidates from Gentile Fusillo et al. (2021), and cross-matched with the *TESS* telescope data for objects up to magnitude $G = 17.5$. This process yielded a sample of 9285 stars. We analyze the 21 832 light curves available for all 9285 white dwarfs observed with *TESS* from sectors 1 (starting 25 July 2018) to 69 (ending 20 September 2023). We used the *Lightkurve* package (Lightkurve Collaboration et al. 2018) to download the photometric data observed by *TESS*. We selected the data taken with a cadence of 120 s (and 20 s when available) and processed using the SPOC pipeline (Caldwell et al. 2020). *TESS* telescope observes each sector for 27 days interrupting the observation each ~ 13 days - or less - to send the data to Earth. Due to these gaps in the light curve, we searched for stable variability only up to 12 days. To avoid including pulsation periods, we also checked linear combinations and whether the temperature of the candidate star with periods shorter than 1500 s matched the temperature range of the DOV, DBV, and DAV/ELMV white dwarf instability strips.

We combined the light curves of all sectors in which the star was observed and performed a complete Fourier transform (FT) on it. We also computed the false alarm probability (fap) of 1/1000, that is, the limit beyond which peaks on the Fourier transforms have less than one chance in 1000 of being noise. We use this detection limit to define whether the observed signal is significant. The fap is computed by randomizing (Monte Carlo-like simulation) the observed timings, as described in Kepler (1993). If the FT exhibited any peak with an amplitude above the detection limit, we considered the period with the highest amplitude as a potential variability signal of the WD. When confronted with the detection of multiple harmonic frequencies in the FT, we analyzed the shape of the dips in brightness and examined the light curve folded in phase. When a noisy light curve hindered the observation of the variability curve shape, our approach was to select the harmonic peak with the lowest frequency. Following these criteria, we compile a target list of 843 WDs with a detected variability frequency.

We identified within the WDs composing our sample those with magnetic field detected, as well as those in binary systems. For magnetic WDs, we first used the classification from Amorim et al. (2023) catalog and then the literature for other objects (e.g., McCook & Sion 2016; Wenger et al. 2000; Kepler et al. 2021; O’Brien et al. 2023; Tremblay et al. 2020; Kilic et al. 2020; Guo et al. 2022). For WDs in binary systems, we consulted the literature above and detected new ones, inspecting the proper motion and parallax of the stars within a box of $120''$ around the white dwarf.

1.1. Localizing the signal

The *TESS* telescope offers long-time light curves and high-frequency resolution. However, due to its large plate scale of $21''\text{px}^{-1}$, it exhibits a low spatial resolution. Consequently, signals from nearby sources contaminate many *TESS* light curves. We overcome this problem using *TESS-Localize* software (Higgins & Bell 2023) to determine whether the detected period arises from the WD or a nearby star. For each star in our target list, we run *TESS-localize* for all sectors in which the star was observed, setting the *Principal Components* parameter to 3 (see Higgins & Bell 2023).

There are two crucial *TESS-Localize* output parameters that need to be checked to ensure the quality of the fit: *Height* and *p-value*. When *TESS-Localize* fits the signal positions, the strength of the signals is represented as the best-fit *Height* parameter. Similarly to the challenge of identifying stars in an image, the signal needs to stand out significantly from the background noise. Higgins & Bell (2023) recommends that the *Height* parameter exceed five times its uncertainty for the localization to be considered significantly above the noise floor. Another critical parameter is the *p-value*; this number supports the hypothesis that the fit location of the signal is consistent with the source position. For we do not discard this hypothesis, the *p-value* should be reasonably high. We adopt the same threshold as Pedersen & Bell (2023): '*p-value*' ≥ 0.05 . Applying these criteria, we selected only those sectors for which *TESS-Localize* achieved a significant localization of the signal of interest that is consistent with the location of a known *Gaia* source brighter than $G = 18\text{ mag}$. Therefore, as we excluded noisy sectors, we do not need to be concerned about the variation in noise from sector to sector.

The final constraint step involves an examination of the *Relative Likelihood*, also an output parameter of *TESS-Localize*. It essentially ranks the proximity of *Gaia* sources to the localized position of the signal within the pixels. For the same target, *TESS-Localize* can fit distinct values of *Relative Likelihood* for each available

sector of data. So, for analysis purposes, we denoted the mean *Relative Likelihood* over all selected sectors as *Like*. To be consistent, we only consider that the signal originates from the WD if *TESS-Localize* indicates the WD as the most probable source for all selected sectors. To demonstrate the consistency of our results, we imposed different thresholds on *Like* and *Amplitude* of the detected signals, creating four distinct samples. Given that the software estimates $Like \simeq 0.75$ for some known variables (see Appendix A - Known RR Lyrae Star), *Sample 1* was selected by applying $Like \geq 0.75$. One might think 75% is not enough, so we propose *Sample 2* with a stricter criterion on *Like*, selecting only candidates with $Like \geq 0.99$. *Sample 3* was chosen considering the fact that *TESS-Localize* was tested only for signals with an *Amplitude* greater than 7σ (7 times the mean *Amplitude* of the FT). Lastly, to affirm the reliability of our finding, even considering just extremely high variability, we selected *Sample 4* imposing an even more rigorous *Amplitude* criterion of 10σ .

The *TESS-Localize* analysis with strict conditions reduced by 70% our initial sample of 843 candidate stars. *Sample 1* consists of 267 WD, including 64 in binary systems and 15 that have detected magnetic fields. Further details of the samples are available in Table 1, which summarizes information on the applied selection thresholds, the quantities of white dwarfs, binaries, and magnetic stars in each sample, along with their median periods. Table 4 in Appendix C - Rotational Periods Table lists all stars that compose our samples, informing its variability period, amplitude, *Like*, mean *Height* parameter normalized by uncertainty, temperature, mass, and additional information. Table 4 also reports the fraction of sectors whose *TESS-Localize* fit achieved our quality criteria as '*Q/S*'.

For 5 of the 267 WDs in our sample, the variabilities detected in *TESS* data have already been reported by Farihi et al. (2023). They are 'TIC 328029653', 'TIC 251080865', 'TIC 251903434', 'TIC 204440456' and 'TIC 321979116'. The reported periods are in agreement with our findings. They claim that the variability found in WD2138-332 data (TIC 204440456) is the stellar rotation period almost certainly due to magnetism.

2. RESULTS

In this section we present the results for the rotation period distribution for the 267 WDs. Assuming that any inhomogeneity on the stellar surface will manifest itself as variability with the rotation period of the surface, from now on, we will attribute the detected variability periods to rotation. This consideration follows the exclusion of all periods potentially caused by pulsation.

	Thresholds	Stars	Binaries	Magnetic	Median Period (h)
<i>Sample 1</i>	$Like \geq 0.75$	267	64	15	7.30
<i>Sample 2</i>	$Like \geq 0.99$	243	52	15	6.92
<i>Sample 3</i>	$Like \geq 0.99$ and Amplitude $\geq 7\sigma$	197	49	9	7.99
<i>Sample 4</i>	$Like \geq 0.99$ and Amplitude $\geq 10\sigma$	164	45	6	7.90

Table 1. Compilation of our samples information: their stellar composing, the thresholds used to select them, and their median period.

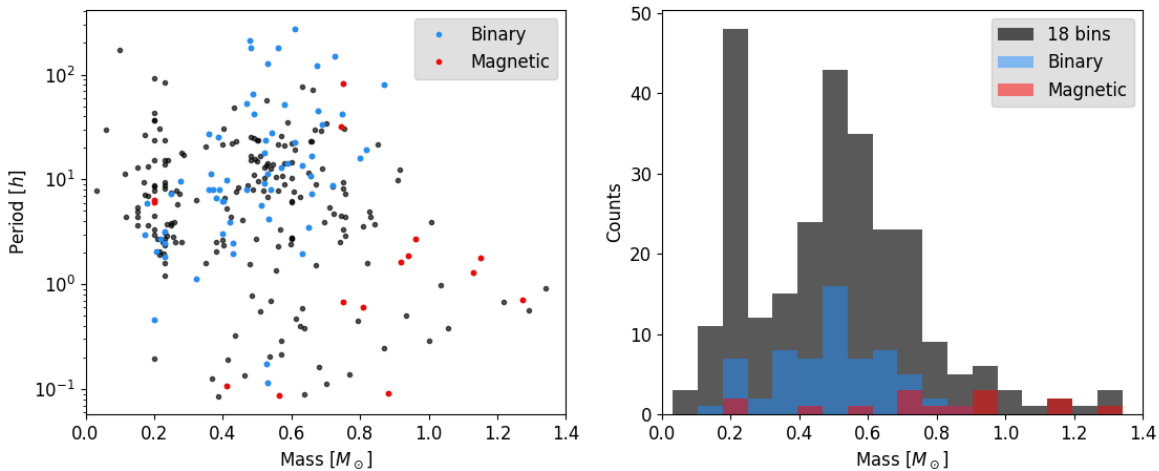


Figure 1. The left panel displays the rotational period in hours in log scale versus mass in solar masses, while the right panel shows the mass distribution of sample 1. The red dots/bins represent magnetic, while blue represents white dwarfs in binary systems, respectively.

273 As mentioned in [Introduction](#), we expect that the ro-
 274 tation period and the orbital period for binary systems
 275 with orbital periods shorter than 17 days are synchro-
 276 nized. Therefore, since the observed periods are shorter
 277 than 12 days, we assumed that all binary systems in
 278 our sample are synchronized.

279 2.1. Mass and Temperature Distribution

280 As the *Sample 1* encompasses all others, we will use it
 281 as a reference sample to analyze the mass and temper-
 282 ature distributions. Figures 1 (2) show the dependence
 283 of the rotation period -in a logarithmic scale- with the
 284 stellar mass (effective temperature), in the left panel,
 285 and the histogram of the period distribution in the right
 286 panel. The red points and bins denote magnetic WDs,
 287 while the blue ones correspond to WDs in binary sys-
 288 tems.

289 The histogram in Figure 1 shows a distribution centered
 290 around approximately $0.6 M_{\odot}$ and, standing out
 291 from this distribution, there is the $0.2 M_{\odot}$ bin (the
 292 highest). The distribution around $0.6 M_{\odot}$ is consis-
 293 tent with the values expected for WD mass distribution
 294 (O’Brien et al. 2023). On the other hand, the high bin
 295 at $0.2 M_{\odot}$ contains 18% of the sample and cannot be

296 explained by single evolution. WDs with a mass lower
 297 than $0.45 M_{\odot}$ are formed by binary interaction (e.g.
 298 Marsh et al. 1995; Kilic et al. 2007) since it would take
 299 longer than the age of the universe for them to evolve
 300 as single stars. Therefore, the high bin at $0.2 M_{\odot}$
 301 indicate a high concentration of WD in binary systems,
 302 which often show photometric ellipsoidal variations at
 303 twice the orbital frequency due to tidal distortion of the
 304 primary (Hermes et al. 2014). It is also important to
 305 note that there is a selection effect on the determina-
 306 tion of the mass. WD spectrum contaminated by an
 307 unresolved red star commonly leads to a mass determi-
 308 nation of approximately $0.2 M_{\odot}$. If this is the case, the
 309 prominent bin at $0.2 M_{\odot}$ in our mass distribution can
 310 be overestimated. However, the conclusion is still the
 311 same: our sample presents a concentration of binaries
 312 larger than we detected. This is not surprising, as the
 313 flux variation caused by binary orbital motion is much
 314 more intense than that caused by spots and patches at
 315 the stellar surface.

316 Even with that in mind, the left plot of Figure 1 shows
 317 that short periods are not dominated by low-mass WDs.
 318 Instead, they are distributed around the entire mass
 319 range of WDs. The low-mass WDs exhibit a wide range

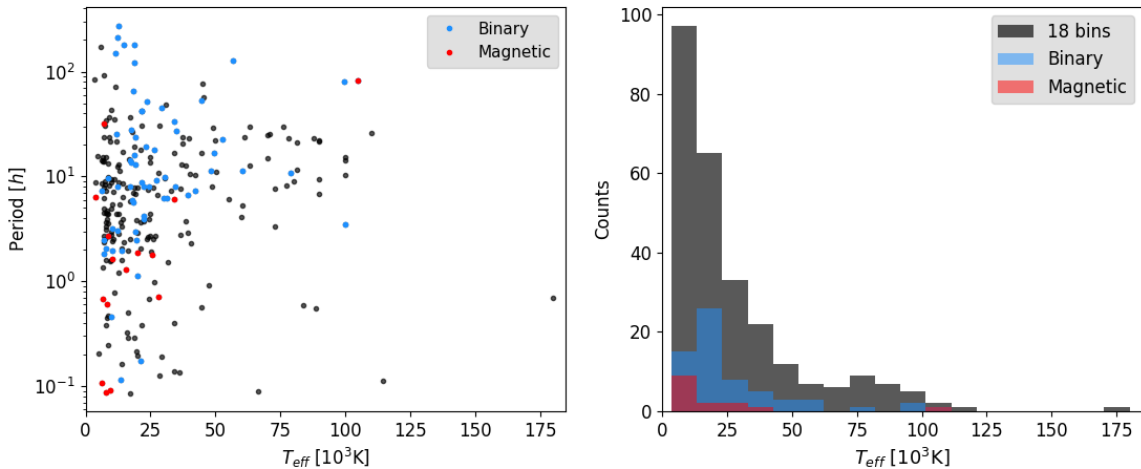


Figure 2. The left panel displays the rotational period in hours versus the effective temperature in Kelvins, both in log scale. The right panel shows the temperature distribution of sample 1. The red and blue dots/bins represent magnetic and binary white dwarfs, respectively.

of rotation periods, spanning from approximately 100 hours to less than 1 hour. Actually, we observe this variety of rotation periods along almost the entire mass range, except for masses larger than $\sim 1M_{\odot}$, where we have few targets.

The left panel of Figure 1 also shows that most magnetic WDs of our sample exhibit periods shorter than 7 h and that they are among the targets with the shortest periods. It is essential to recognize that our sample has selection effects. According to Brinkworth et al. (2013), the rotational period of magnetic white dwarfs exhibits a bimodal distribution, with one group showing periods on the order of minutes to hours and the other displaying periods much longer than their 4 years. However, their total sample is made up of only 26 stars. The observation cycle of the *TESS* telescope lasts ≈ 27 days, with a data transfer interruption in the middle, limiting the detection of periods to a few hundred hours. In this way, we are detecting an unrepresentative portion of magnetic WDs. Furthermore, massive WDs are fainter and tend to rotate faster (e.g., Hermes et al. 2017b; Caiazzo et al. 2021; Williams et al. 2022). Although *TESS* is a small telescope, most of our magnetic sample consists of massive white dwarfs rotating with periods shorter than 3 hours, as Figure 1 shows.

Figure 2 shows that our sample of white dwarfs is distributed around approximately 12,000 K, a representative value of the DA population, which comprises about 80% of the WDs spectroscopically identified (REFERENCE). The left panel of Figure 2, shows that there does not appear to be a dependence of the rotation period with the effective temperature.

Furthermore, there is no obvious dependence of the rotation period with the stellar mass nor the effective temperature of the white dwarf for binary systems. On the other hand, despite the selection effects, magnetic white dwarfs in our sample tend to be located at a higher mass and lower temperatures, probably due to their longer cooling times (Kepler et al. 2021).

2.2. Rotation Period Distribution

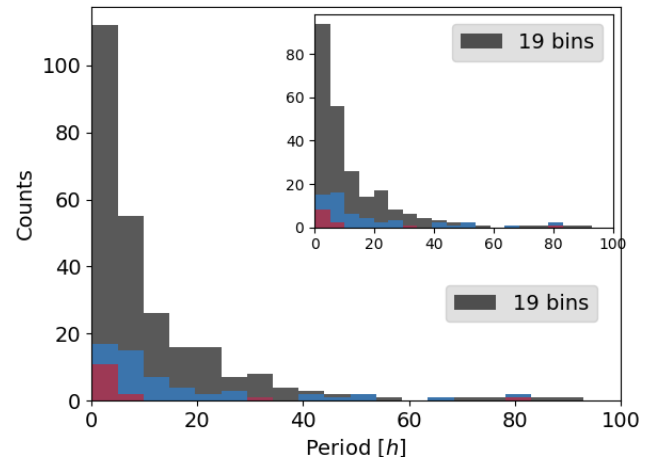


Figure 3. Rotation period histogram of sample 1. The inset plot illustrates the rotation period histogram excluding periods shorter than 0.3 h. Blue bins indicate WD in binary systems, and red bins indicate magnetic WDs.

Figure 3 shows the distribution of rotational periods for sample 1 up to 100 h. As explained in section 1, we excluded pulsation periods. However, to eliminate

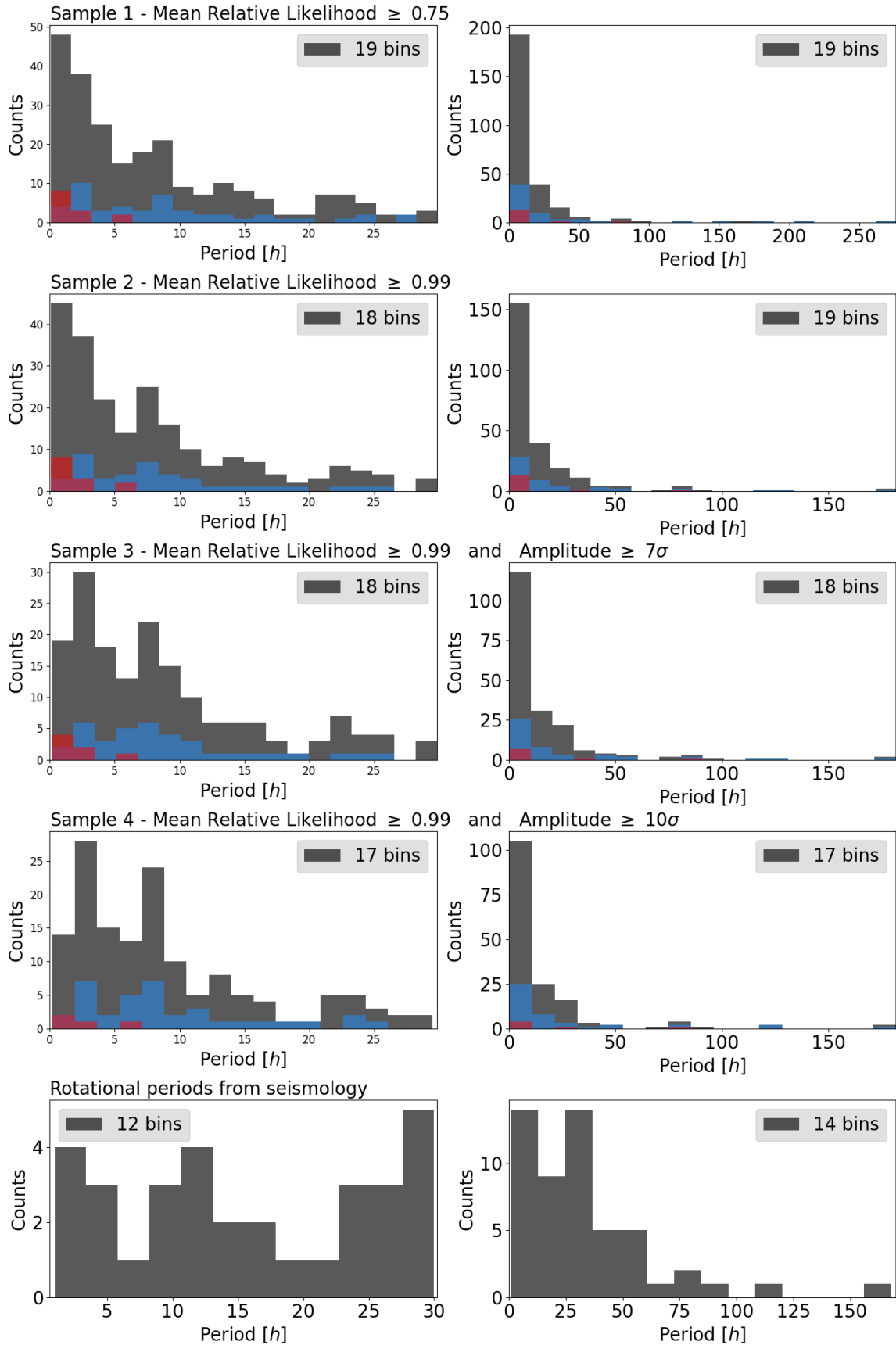


Figure 4. Rotation period histograms for different thresholds over *TESS* data and, last line, histograms of rotation periods from seismology. On the left, we present the histograms of rotation periods up to 30 h, and on the right, the complete histograms. The red and blue bins show, respectively, the binary and magnetic population in our sample of WDs.

any doubts about the short periods in our sample, the inset of Figure 3 shows the histogram of periods longer than 0.3 h. It is important to note that massive white dwarfs can exhibit rotation periods shorter than 0.3 h (e.g. Caiazzo et al. 2021; Barstow et al. 1995). The inset plot confirms that even if we are quite conservative, most of our sample still has rotation periods shorter than 10 h.

Figure 4 shows the complete histograms of the rotational periods (right) and the histograms of periods up to 30 h (left) for our four samples. Each line of this figure displays the histograms of one sample, indicated by the respective subtitles. The first line presents the histograms of *Sample 1*, the second line presents the histograms of *Sample 2*, and so on. The last line of Figure 4 shows the same histogram but for the rotational periods determined through asteroseismology, which are listed in Table 2. The red and blue bins represent the magnetic WDs and the WD in binary systems.

The right panels of Figure 4 show that more than 60% of the targets fall into the shortest period bin for all four of our samples. It shows that regardless of the restrictions chosen on our initial sample, the data remain indicating the same result: most WDs have a rotational period shorter than approximately 10 h. The left panels of Figure 4 display the same histograms but periods up to 30 hours. They show that the stricter the threshold over the sample, the more prominent the distribution of periods around three distinct values: approximately 3 h, 8 h, and 24 h.

Looking at the right panel of the last line, we see that the distribution of the seismological periods is a little different from the distributions of our samples. Despite the smaller sample size, its shortest period bin is not as prominent as we observed in the distributions of our samples. Instead, the seismological distribution presents almost as many periods shorter than 13 h (14) as periods between 25 and 37 hours (13). The seismological histogram presents a bimodal distribution around the first bin (periods shorter than 13 hours) and approximately 31 hours. Looking at the short periods, the last line of Figure 4 reveals that the asteroseismological periods are also distributed around three values. Similarly to those observed in our samples, the seismological histogram is distributed around approximately 2 h, 12 h, and 31 h.

Figure 4 also shows that the fraction of WD in binary systems with periods shorter than 30 h increases as we restrict our sample. Looking at the binary’s period distribution, they do not exhibit a preferential value; instead, they are evenly distributed. It is challenging to draw definitive conclusions about magnetic white dwarfs due to the small sample size. Despite this limitation,

Figure 4 points in the direction where magnetic WDs tend to be fast rotators since most present rotational periods are shorter than 6.4 h.

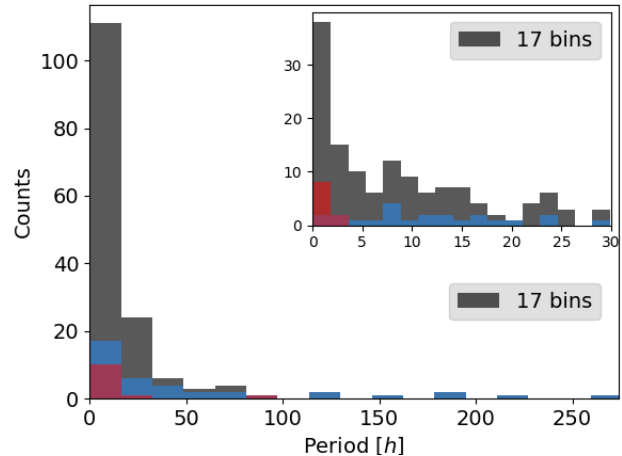


Figure 5. Rotation period histogram of sample 1 excluding target stars with a mass lower than $0.45 M_{\odot}$. The principal plot illustrates the entire histogram of rotation periods and the inset plot the histogram with periods up to 30 h. Blue bins indicate WD in binary systems, and red bins indicate magnetic WDs.

Figure 5 shows the distribution of rotational periods only stars with mass higher than $0.45 M_{\odot}$. The principal plot presents the entire histogram of periods, while the inset plot presents the histogram for periods up to 30 h. This plot confirms, that even if the variability we found for the low-mass WDs were all due to ellipsoidal variations, this is not what is causing the short periods in our samples. Contrarily, Figure 5 shows that excluding the low-mass WDs from our sample emphasized the salience of the shortest period bin.

2.3. Rotation periods from asteroseismology

As mentioned in Introduction, Kepler & Romero (2017), Hermes et al. (2017b) and Kawaler (2015) studied the rotation period of WD using determinations from asteroseismology analysis. Extending their work, we compile all 53 WDs stars with reported seismological rotation periods up to the present. They are listed in Table 2. We have already shown the histogram of the seismological periods in Figure 4, they present a median rotational period of 27 hours and a standard deviation of 30 hours. Investigating the trend of decreasing rotation period with increasing white dwarf mass claimed by Hermes et al. (2017b), we present Figure 6 that shows the rotation period versus mass relation for the seismological sample. The current plot does not show this trend,

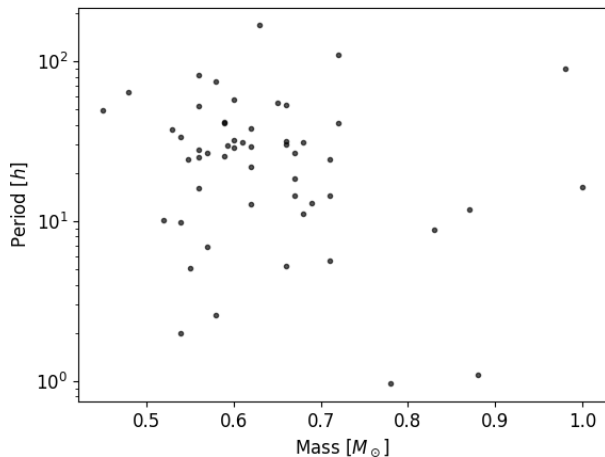


Figure 6. Rotation period versus mass relation for period determinations from asteroseismology. The period axis is in log scale.

443 instead the two most massive stars in our sample exhibit
444 rotation periods longer than 10 hours.

2.4. Ground-based observations

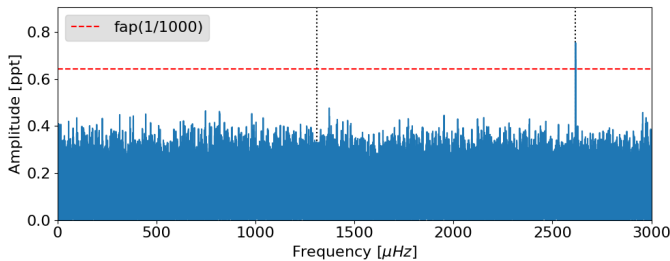


Figure 7. Fourier Transform of *TESS* data of star 'TIC262548040'. The horizontal red line indicates the false alarm probability and the vertical dotted lines indicate the peak of 0.106 *h* and its double.

446 [Moss et al. \(2023\)](#) observed two magnetic WD from
447 our sample from a ground-based telescope. They
448 detected a rotation period of 0.648 *h* for the star
449 'TIC392797216' (LHS 2273), which is very close to the
450 period of 0.68 *h* we found in *TESS* data. They also
451 observed the 'TIC262548040' star (LHS 1243), detect-
452 ing a rotation period of 0.216 *h*. Figure 7 presents the
453 FT of the data obtained by *TESS* for this star, showing
454 that only one peak at 2617 μHz (0.106 *h*) is above the
455 false alarm probability (horizontal red line). The dotted
456 horizontal lines indicate the peak of 0.106 *h* and its double,
457 showing that there is no significant peak at 0.212 *h*
458 of *TESS* data. Therefore, we can only detect the har-
459 monic frequency in *TESS*, but the real rotation period is

460 0.212 *h*. Despite the harmonic issue, [Moss et al. \(2023\)](#)
461 confirms the rotation rate for two of the fastest rotators
462 in our sample.

3. EVOLUTIONARY MODELS

463
464 As we are studying the rotation rates of evolved white
465 dwarf stars, assuming that the zero-age main-sequence
466 models do not have differential rotation, one question
467 that arises is how the evolution changes the internal ve-
468 locities and how much of the initial angular momentum
469 is lost during the expressive mass loss phase of AGB
470 before the white dwarf phase.

3.1. Observational and modeling context

471
472 Using ground-based photometric observations time se-
473 ries from main sequence stars spanning from late-F to
474 early-M spectral types, [Fritzewski et al. \(2021\)](#) deter-
475 mined 279 rotation periods for members of the 300 Myr-
476 old open cluster NGC 3532. They found that the ro-
477 tation periods range from 0.5 *d* to 32 *d*, with trends
478 of slow-rotating FGK stars and fast-rotating K dwarfs.
479 In another recent investigation, [Labadie-Bartz et al.](#)
480 (2023) explored the rotational characteristics of chemi-
481 cally peculiar (CP) stars located in the upper main se-
482 quence, utilizing *TESS* data. Among their findings is
483 that the rotation period distribution of CP stars is cen-
484 tered around 3 days. CP stars are observed within the
485 spectral types from early B to early F. Since all stars
486 with spectral type roughly from A to K will become
487 WDs and we have demonstrated in this work that the
488 median rotation period of WD is around 7 *h*, these find-
489 ings suggest that a robust mechanism of internal angular
490 momentum transfer operates during the evolution of the
491 WDs progenitors.

492 Studying the internal rotation rates for hundreds of
493 main-sequence stars in Gamma Doradus, [Moyano et al.](#)
494 (2023) concluded that the transport of angular momen-
495 tum in radiative zones during the main sequence of low-
496 mass stars must be efficient, and the internal magnetic
497 fields are a strong candidate for the missing physical in-
498 gredient in stellar interiors. In addition, they point out
499 that at least one efficient process able to neutralize the
500 development of differential rotation in stellar interiors
501 must act during the whole evolution of this type of star.
502 Comparisons between models and asteroseismic deter-
503 minations of core rotation rates for low- and
504 intermediate-mass stars during evolved phases, high-
505 lighted the need for varying efficiencies of internal an-
506 gular momentum transport in different mass ranges to
507 match observations ([Moyano et al. 2022](#)). [Moyano et al.](#)
508 (2023) highlighted the importance of efficient angular
509 momentum transport, possibly involving internal mag-

Star	P_{seism} [h]	Type	Mass [M_{\odot}]	Ref.	Star	P_{seism} [h]	Type	Mass [M_{\odot}]	Ref.
TIC 7675859	5.2	DAV	0.66	1	TIC 343296348	24.48	DAV	0.548	1
TIC 21187072	53.76	DAV	0.66	1	TIC 394015496	29.76	DAV	0.593	1
PG 1159-035	33.6	DOV	0.54	2	RX J2117.1+3412	25	DOV	0.56	3
GD133	168	DAV	0.63	4	EPIC220274129	12.7	DAV	0.62	5
PG 0112+104	10.2	DBV	0.52	6	KIC 4552982	18.4	DAV	0.67	7
KIC 4357037	22	DAV	0.62	7	KIC 7594781	26.8	DAV	0.67	7
KIC 10132702	11.2	DAV	0.68	7	EPIC60017836	6.9	DAV	0.57	7
EPIC201719578	26.8	DAV	0.57	7	EPIC201730811	2.6	DAV	0.58	7
EPIC201802933	31.3	DAV	0.68	7	EPIC210397465	49.1	DAV	0.45	7
EPIC211596649	81.8	DAV	0.56	7	EPIC211629697	64	DAV	0.48	7
EPIC211914185	1.1	DAV	0.88	7	EPIC211926430	25.4	DAV	0.59	7
EPIC228682478	109.1	DAV	0.72	7	EPIC229227292	29.4	DAV	0.62	7
EPIC220204626	24.3	DAV	0.71	7	EPIC220258806	30	DAV	0.66	7
EPIC220347759	31.7	DAV	0.66	7	EPIC201806008	31.3	DAV	0.61	7
KUV02464+3239	90.7	DAV	0.98	8	SDSS J0349-0059	9.8	DOV	0.54	9
GD 165	57.3	DAV	0.6	10	Ross 548	37.8	DAV	0.62	10
PG1707+427	16	DOV	0.56	11	WD 1711+657	16.4	DAV	1.00	11
GD 358	29	DBV	0.6	11	G29-38	32	DAV	0.6	11
EC20058-5234	2	DBV	0.54	11	EC14012-1446	14.4	DAV	0.71	11
KIC 11911480	74.7	DAV	0.58	12	WD 0937+010	11.8	DAV	0.87	13
SDSS J1612+830	0.96	DAV	0.78	13	KUV11370+4222	5.7	DAV	0.71	14
GD 154	55.2	DAV	0.65	15	HS 0507+0434	40.9	DAV	0.72	15
KIC 8626021	40.8	DBV	0.59	16	PG 0122+200	37.2	DOV	0.53	17
HL Tau 76	52.8	DAV	0.56	18	G185-32	14.5	DAV	0.67	19
L19-2	13.0	DAV	0.69	20	LP 133-144	41.8	DAV	0.59	21
NGC 1501	28.1	DOV	0.56	22	G226-29	8.9	DAV	0.83	23
PG 2131+066	5.1	DOV	0.55	24					

Table 2. White dwarfs with rotation periods determined previously by asteroseismology.

References: (1)Romero et al. (2022);(2)Oliveira da Rosa et al. (2022); (3)Córscico et al. (2021);(4) Fu et al. (2019);(5) Bell et al. (2017); (6) Hermes et al. (2017a); (7) Hermes et al. (2017b); (8) Li et al. (2017); (9) Calcaferro, Leila M. et al. (2016); (10) Giammichele et al. (2016); (11) Kawaler (2015); (12) Greiss et al. (2014); (13) Castanheira et al. (2013); (14) Su et al. (2013); (15) Fu et al. (2012); (16) Østensen et al. (2011); (17) Fu, J.-N. et al. (2007); (18) Dolez, N. et al. (2006); (19) Pech, D. & Vauclair, G. (2006); (20) Bradley (2001); (21) Pfeiffer et al. (1996); (22) Bond et al. (1996); Kepler et al. (1995); (23) Kawaler et al. (1995).

510 netic fields, throughout the main-sequence evolution of
511 low-mass stars.

512 3.2. Our models

513 We computed evolutionary sequences using the Mod-
514 ules for Experiments in Stellar Astrophysics code (MESA,
515 Paxton et al. 2011, 2013, 2015, 2018, 2019; Jermyn et al.
516 2023), release 22.11.1. Our models have an initial mass
517 of $M_i = 1.5 M_{\odot}$ and an initial metallicity of $Z = 0.02$,
518 0.002 and 0.001. They are computed from the zero-age
519 main sequence (ZAMS) until a white dwarf cooling effec-
520 tive temperature of 8500 K. Our models start with equa-
521 torial surface rotation velocities of 10 and 50 km s⁻¹.
522 These values are assumed to be the solid-body rotations

523 at the ZAMS. The initial mass was chosen to be above
524 the $1.3 M_{\odot}$ lower limit for the convective core in the
525 main sequence (e.g. Aerts & Tkachenko 2023). For fur-
526 ther information about the models see Appendix B -
527 Evolutionary Models Input.

528 The mixing of elements and the transport of angular
529 momentum due to rotation are implemented in MESA
530 following closely Heger et al. (2000, 2005). Two effi-
531 ciency factors must be set to calibrate the diffusion co-
532 efficients: the contribution of rotationally induced in-
533 stabilities to the diffusion coefficient is reduced by the
534 factor $f_c = 1/30$, and the sensitivity of rotationally in-
535 duced mixing is $f_{\mu} = 0.05$. We consider the following
536 angular momentum transport mechanisms: Dynamical

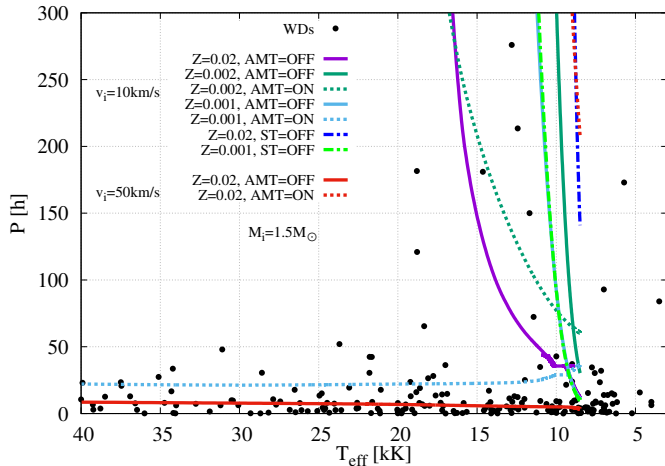


Figure 8. Observational data of the surface rotation of white dwarf stars (black dots) are compared against evolutionary models showing the rotation period in the white dwarf cooling track. We compare models with the six mechanisms of angular momentum transport turned off (solid lines) and on (dotted lines) during the whole evolution. For initial rotational velocity of $v_i = 10 \text{ km s}^{-1}$, we present models with metallicities of $Z = 0.02$ (purple), 0.002 (dark green), and 0.001 (light blue). We also compare two models where the Spruit-Tayler dynamo is the only mechanism turned off during the computations (dark blue and light green dotted-dashed lines). For an initial rotational velocity of $v_i = 50 \text{ km s}^{-1}$, we compare two models with $Z = 0.02$ (red lines). All model sequences have an initial mass of $1.5 M_{\odot}$.

shear instability, Solberg-Hoiland, secular shear instability, Eddington-Sweet circulation, Goldreich-Schubert-Fricke and the Spruit-Tayler dynamo.

The final masses of our models are $0.546 M_{\odot}$ for $Z = 0.02$, $0.577 M_{\odot}$ for $Z = 0.002$, and $0.585 M_{\odot}$ for $Z = 0.001$. This aligns with expectations that stars with higher metallicity should form less massive CO cores (and therefore lower final mass) and lose more mass in the AGB phase than stars with the same initial mass but lower metallicity (e.g., Dominguez et al. 1999; Catalán et al. 2008; Romero et al. 2015; Choi et al. 2016). Similar models with initial masses of $2.5 M_{\odot}$ reach the white dwarf phase with masses around $0.6 M_{\odot}$.

In Figure 8 we show the evolution of the surface rotational period (P) versus the effective temperature (T_{eff}) during the cooling track for a set of model sequences with different metallicity and initial rotation velocity. The surface rotational period is computed via $P = 2\pi r/v$, where r is the model radius and v is the rotational velocity at the equator. Sequences that consider the six mechanisms of angular momentum transport are shown as dotted lines (AMT=ON), and the solid lines represent sequences with all the mechanisms turned off (AMT=OFF).

For $v_i = 10 \text{ km s}^{-1}$ and $Z = 0.02$ (purple line in Figure 8), we find that the models with AMT = OFF decrease the average equatorial rotation period on the surface from $P = 300 \text{ h}$ to $\sim 30 \text{ h}$ when cooling from $\sim 17 \text{ kK}$ to 8500 K . The sequence with AMT=ON does not even reach 300 h before cooling down to the same temperature (and therefore does not appear in the plot).

For sequences with $Z = 0.002$ (dark green lines in Figure 8), we find that if AMT=OFF (solid line), the models brake from $P = 300 \text{ h}$ to 40 h only at the very end of the cooling track ($T_{\text{eff}} < 10 \text{ kK}$), while the AMT=ON sequence (dotted line) has already spun down to 300 h when $T_{\text{eff}} < 17 \text{ kK}$, although it reaches only $P \sim 60 \text{ h}$ at $T_{\text{eff}} = 8500 \text{ K}$.

Since the internal redistribution of the angular momentum is very efficient early in the evolution of low-mass stars (e.g., Mosser et al. 2012), This suggests that when AMT=ON, a large amount of mass lost by winds during the AGB phase carries away most of the angular momentum, and thus, the surfaces of the models rotate slower in the WD phase.

The difference in turning the angular momentum transport mechanisms on and off is much more pronounced for low metallicity. ($Z = 0.001$, light blue in Figure 8). While AMT=OFF (solid line) follows the same trend as for higher metallicities (i.e. reaching low P only at the end of the cooling track), the sequence with AMT=ON (dotted line) cools from $T_{\text{eff}} = 40,000 \text{ K}$ down to 8500 K with approximately constant rotation period of $P = 25 \text{ h}$, closer to most of the observed period distribution.

In Figure 8 we also show two sequences of models with $v_i = 10 \text{ km s}^{-1}$ where the Spruit-Tayler mechanism was turned off, and all the other five mechanisms were kept on during the whole evolution (ST=OFF, dotted-dashed lines). For $Z = 0.001$ (light green line), the result is similar to that of the same metallicity but with all six angular momentum transport mechanisms turned off. This suggests that the Spruit-Tayler mechanism dominates over the other mechanisms from the point of view of the rotation analysis during the WD phase.

Finally, we present two sequences with $v_i = 50 \text{ km s}^{-1}$ and $Z = 0.02$. These models show that observational data with a shorter rotation period ($P < 50 \text{ h}$) are better adjusted by models with AMT=OFF, while models with AMT=ON present a rotation period shorter than 300 h only at the end of white dwarf cooling when $T_{\text{eff}} < 10,000 \text{ K}$. This suggests that if we disregard the Spruit-Tayler mechanism throughout the evolution, models with a higher initial velocity (50 km s^{-1}) fit the white dwarf rotation data better if the initial mass is $1.5 M_{\odot}$.

4. CONCLUSION

Assuming the variability detected in the *TESS* data is caused by rotation, Table 1 shows that, independently of the applied selection thresholds, the most probable rotational period of WDs is about 7 h. The right panels of Figure 4 show that, for all samples, more than 60% of the stars present periods shorter than approximately 10 h. The stricter the sample, the more prominent the distribution of the rotational periods of the WD around three different values: approximately 3 h, 8 h, and 24 h. This result agrees with the distribution of rotational periods from seismology, which also presents a similar pattern. Detecting periods shorter than approximately 12.5 h through seismology is less frequent than our findings. Consequently, the seismological sample shows a higher median rotational period of 27 h and a standard deviation of 30 h. For the ground observations, there is a selection bias that observations last in general 3 to 4 h, limiting the frequency resolution. The similarity of the period distribution of our samples and the seismological period distribution is a good indicator that our samples represent the rotation rate of WDs.

The figures presented in Section 2 indicate that binary WDs do not exhibit a preferential mass, temperature, or period. However, despite the small sample, magnetic WDs are preferentially massive, cool, and fast rotators.

As discussed in Section 2.1, Figure 1 might indicate a large concentration of WDs formed in interacting binary systems. However, this does not mean that these stars are still in binary systems, nor that detected variability comes from orbital motion. Figure 1 also shows that the short periods (shorter than 10 h) are not restricted to low-mass WD, instead, they are distributed through the entire mass range. Even if we assume that all WDs in our sample with mass lower than $0.45M_{\odot}$ are in binary systems and that the variabilities we detected are due to ellipsoidal variation, it does not change our findings. Figure 5 shows that the rotation period histogram excluding the low-mass WDs remains the same: periods shorter than 10 h are by far the most common. Therefore, this Figure reaffirms that the hundred short rotation period stars we detect are not related to the large concentration of low-mass WDs in our sample.

It is important to note that we are not negating that there are WDs in binary systems composing our sample. We know that there are and we are assuming that their orbital period is synchronized with the rotation period. In both cases, single and binary systems, we may be detecting and reporting half-period aliases. Moss et al. (2023) confirmed the rotation period we detected in *TESS* data for two of the fastest rotators in our sample. Using ground-based observations, they detected rotation

periods very close to our findings, but also provided an example of half-period aliases. For 'TIC262548040', we only detect in *TESS data* the harmonic of the real rotation period. Without the ground-based observations of Moss et al. (2023), we would not be able to know that the signal we detected is a harmonic frequency. Therefore, we may be detecting and reporting half of the real rotation period for other stars. However, it does not invalidate our findings, since the same work confirmed rotation periods of 0.68 h and 0.21 h for two magnetic WDs in our sample.

Most of the stars in our sample that exhibit rotation periods shorter than 50 h present effective temperature lower than 40 kK. Figure 8 presents two models that at 40 kK reach rotation periods consistent with the findings of this work. We find that the periods shorter than 50 h and are well-fitted by models with $Z = 0.02$, $v_i = 50 \text{ km s}^{-1}$ and angular momentum transport set OFF; or by models with $Z = 0.001$, $v_i = 10 \text{ km s}^{-1}$ and angular momentum transport set ON. A smaller part of the observational data presents a large dispersion of the rotation period and is concentrated at $T_{\text{eff}} < 20,000 \text{ K}$. Our remaining models best fit these stars.

While other studies have shown that the internal transfer of angular momentum should be intense in the early phase of the evolution of low-mass stars, our study confirms that if we seek to match most of the white dwarf rotational data, this redistribution should cease or be less intense before the end of the AGB phase, when stars lose the highest amount of mass and, therefore, angular momentum. If we assume that stars with lower metallicity will have a lower mass loss rate due to winds at the top of the AGB phase (e.g., see discussion in Höfner & Olofsson 2018), this means that they will lose less angular momentum and therefore rotate faster in the WD phase. On the other hand, when we consider that more angular momentum transfer mechanisms have been activated since the beginning of the evolution, more angular momentum will be transferred to the surface and lost during the AGB phase. Thus, in terms of the WD rotation period, lowering the metallicity is equivalent to reducing the angular momentum transfer mechanisms in the early evolution. Due to their intrinsic faintness, the observed white dwarfs are mainly near disk objects, most likely with metallicity closer to the Sun's.

In general, our models agree with the most recent results in the literature in the sense that different initial parameters can be used to create models that are in agreement with a particular part of the observational data, but there is a degeneration in the parameter space (i.e., the initial velocity of rotation, initial mass, metallicity, etc.) that could be better resolved if we knew more

717 precisely how the redistribution of angular momentum
718 occurs in stellar interiors.

719 In the future, we will analyze *TESS* data observed
720 after Oct 2023, calculate models with the Fuller dynamo
721 prescription, and extend the mass range of the models as
722 the data includes white dwarfs with a range of masses.

723 This work was carried out with the financial sup-
724 port of the Conselho Nacional de Desenvolvimento
725 Científico e Tecnológico (CNPq), by the Coordenação de
726 Aperfeiçoamento de Pessoal de Nível Superior - Brasil
727 (CAPES). This research has made extensive use of
728 NASA’s Astrophysics Data System Bibliographic Ser-
729 vice (ADS), and SIMBAD.

730 APPENDIX

731 APPENDIX A - KNOWN RR LYRAE STAR

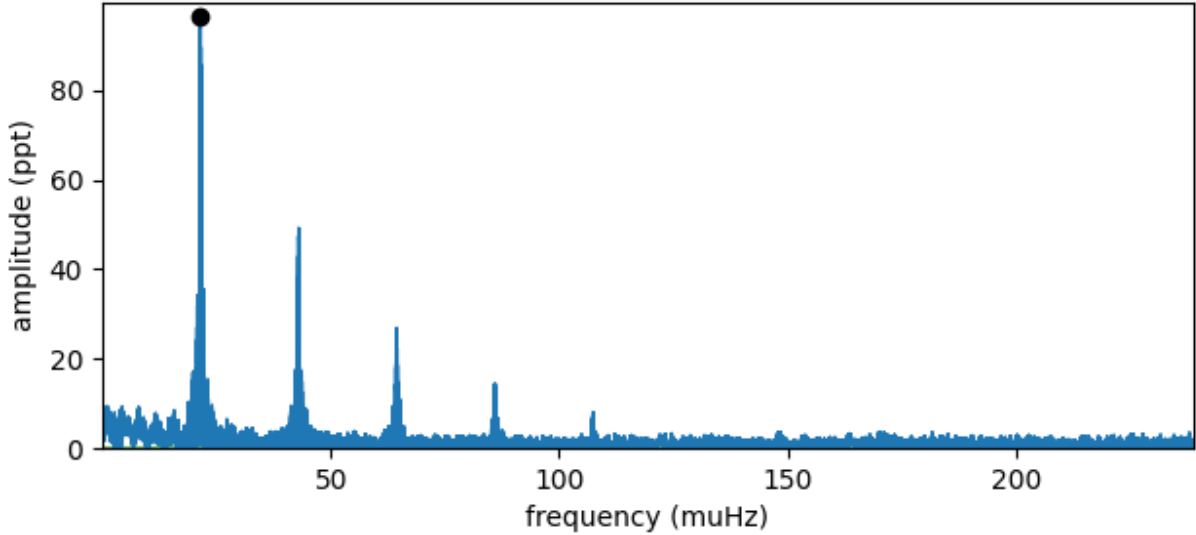


Figure 9. BPM 24754 light curve from sectors 12, 39, and 66.

732 BPM 24754 (TIC 367227831) is a known RR Lyrae variable white dwarf. Figure 9 shows its FT of *TESS* data
733 plotted using the software Pyriod (Bell 2020). In this case, we know that the primary signal at 21.49μ Hz (12.92 h)
734 and its harmonics are the contamination from the known RR Lyrae variable *Gaia DR3 5923100101270979328* (TIC
735 367227833). The results of *TESS-Localize* software for the three sectors where the star is observed (12, 39, and 66)
736 are:

Sector	Source	pvalue	Relative Likelihood	χ^2	Height [σ]
12	'5923100101270979328'	0.214	0.75	44.40	42.40
12	'5923100101249048320'	0.071	0.19	44.40	42.40
39	'5923100101270979328'	0.503	0.83	312.71	17.30
39	'5923100101249048320'	0.191	0.11	312.71	17.30
66	'5923100101270979328'	0.829	0.96	62.47	37.22
66	'5923100101249048320'	0.198	0.03	62.47	37.22

Table 3. *TESS-Localize* results to the signal 12.92 h in present in the light curve of BPM 24754.

737 *TESS-Localize* estimates that the probability that the signal source is the RR Lyra star is 75% in sector 12, even the
738 parameters *pvalue* and *Height* indicating good values. The *Relative Likelihood* of the RR Lyrae star being the source

739 of signal increases in the subsequent sectors, with the mean like reaching 85%. The second source is likely the same for
 740 all three sectors, *Gaia DR3 5923100101249048320*. This object is located 3.06*arcsec* away from the RR Lyrae star.

741 APPENDIX B - EVOLUTIONARY MODELS INPUT

742 Hydrogen and helium burning are computed using the `pp_and_cno_extras.net` network that accounts for 25 isotopes
 743 and 79 net reactions. Convection is treated using the formulation of the mixing-length theory (Böhm-Vitense 1958)
 744 in the variation of Henyey et al. (1965) allowing the convective efficiency to vary with the opacity. We set the diffusion
 745 of elements for the whole net; each isotope in the network is treated as its own class.

746 Following the MIST project (Choi et al. 2016), $\alpha_{\text{MLT}} = 1.82$ is adopted as the mixing length parameter. We consider
 747 the Ledoux criterion of stability, which considers the influence of composition gradients on mixing. Semiconvection is
 748 considered unstable regions by the Schwarzschild criterion but stable by Ledoux, with an efficiency parameter $\alpha_{\text{sc}} = 0.1$.
 749 Thermohaline mixing is included throughout evolution, with efficiency $\alpha_{\text{th}} = 666$.

750 Exponential overshooting is set to $f = 0.008$ in the core and 0.0087 in the shell. We handle mixing in the convective
 751 zones using the convective premixing scheme. For the boundary conditions of the atmosphere, we use the $T(\tau)$
 752 Eddington relation with varying opacity for most of the evolution and hydrogen atmosphere tables for cool white
 753 dwarfs (Rohrman et al. 2011) when the models are on the cooling track and the effective temperature is below
 754 10,000 K. The mass loss by stellar winds is taken into account using the Reimers (1975) scheme with $\eta_{\text{R}} = 0.5$ for the
 755 red giant branch phase and the Bloeker (1995) scheme with η_{B} varying between 0.1 and 1 for the asymptotic giant
 756 branch phase.

757 APPENDIX C - ROTATIONAL PERIODS TABLE

Table 4. Photometric rotation Periods.

TIC	Period [h]	Amplitude [σ]	Like	\langle Height [σ] \rangle	T_{eff} [K]	Mass [M_{\odot}]	Q/S	info
144002497	7.6213 ± 0.0022	48.042	1.00	42.8	72910	0.606	2/2	
837076117	11.468 ± 0.007	7.899	1.00	11.2	81335	0.65	1/2	DA
307982318	$1.53006 \pm 7\text{e-}05$	4.803	1.00	5.0	31880	0.67	1/3	hotDAV
7675859	12.343 ± 0.008	10.018	1.00	8.2	12445	0.917	5/6	DAV
88564975	8.9702 ± 0.003	173.775	1.00	92.9	80000	0.67	3/3	
136884288	0.6053 ± 0.0006	7.730	1.00	13.6	8440	0.81	1/1	DAHe
383647517	13.924 ± 0.014	13.263	1.00	6.2	6754	0.545	7/16	DQpec
1102584065	26.187 ± 0.022	17.910	1.00	9.1	110000	0.57	12/13	DO
436747174	4.166 ± 0.026	290.193	1.00	59.7	22500	0.532	1/1	DA-CV
434196824	3.904 ± 0.023	53.066	1.00	62.4	14491	0.258	1/1	
345265261	3.759 ± 0.022	7.601	1.00	12.2	38780	0.843	1/1	DA
321272216	4.408 ± 0.031	34.385	0.99	40.0	12597	0.117	1/1	
248861930	12.93 ± 0.26	23.353	1.00	28.0	36903	0.521	1/1	DBA
247992671	15.4 ± 0.4	8.742	1.00	10.8	8000	0.23	1/1	
241256067	15.778 ± 0.028	5.352	1.00	6.0	4730	0.495	1/2	DC
124894242	0.32555 ± 0.00017	4.075	1.00	6.9	15919	0.435	1/1	
154942231	4.4236 ± 0.0022	7.839	1.00	6.4	12000	0.15	3/5	
649932200	0.9712 ± 0.0005	31.107	1.00	28.4	26461	1.036	3/3	
52584399	3.801 ± 0.008	112.873	1.00	66.8	19505	0.249	3/3	
1883129777	1.9446 ± 0.0004	143.936	1.00	71.9	16480	0.229	3/3	
1881564044	6.137 ± 0.004	6.042	1.00	7.4	34000	0.2	2/3	DAH
1101460688	23.24 ± 0.03	10.905	1.00	6.9	88000	0.656	2/3	
22014729	7.6477 ± 0.0032	135.408	1.00	55.8	36580	0.44	1/2	
31798074	21.828 ± 0.017	42.369	1.00	5.3	12011	0.398	1/10	
262921847	13.892 ± 0.004	52.290	1.00	20.7	7000	0.23	12/12	
311886800	10.2157 ± 0.0025	32.576	1.00	19.4	100000	0.6	6/6	

TIC	Period [h]	Amplitude [σ]	Like	\langle Height [σ]	T_{eff} [K]	Mass [M_{\odot}]		info
178994042	$0.2138 \pm 7\text{e-}05$	4.400	1.00	5.6	19770	0.57	1/1	
220478684	16.611 ± 0.010	25.143	1.00	12.6	44589	0.483	19/20	
381976323	8.722 ± 0.01	133.547	1.00	45.2	4000	0.2	11/11	
235072034	84.0 ± 4.0	20.540	1.00	10.5	3500	0.23	2/3	
219244444	7.2886 ± 0.0027	245.106	1.00	12.5	6440	0.25	3/5	DA7+M+planet
245834374	33.6 ± 1.8	7.275	1.00	6.8	34210	0.69	1/1	DA+M
85146644	5.317 ± 0.0011	68.977	1.00	51.4	60260	0.41	3/3	
107310223	11.28 ± 0.23	21.505	1.00	30.9	48116	0.366	1/1	DA1+dM
1101900758	2.65191 ± 0.0003	31.335	1.00	21.4	23941	0.398	5/5	
160119816	21.453 ± 0.017	112.794	1.00	43.3	90000	0.56	9/9	
300284179	12.65 ± 0.29	12.426	1.00	13.8	38490	0.54	1/1	
126910998	19.4 ± 0.6	36.753	1.00	54.9	23075	0.819	1/1	DA+M
218971976	6.7081 ± 0.001	263.431	1.00	65.1	39260	0.38	2/2	DA+M
321979116	2.69506 ± 0.00016	92.402	1.00	36.5	8650	0.96	2/2	DAP5.8
183533908	2.55267 ± 0.00024	11.122	1.00	13.6	7638	0.74	1/1	
630539472	1.592 ± 0.004	4.231	1.00	7.4	10027	0.821	1/1	
201255204	6.34 ± 0.03	59.895	1.00	52.0	4000	0.2	2/2	DBH
439917321	12.98 ± 0.28	61.269	1.00	48.6	19193	0.57	1/1	DA+M
55096188	2.75096 ± 0.00021	4.379	1.00	6.5	10000	0.6	2/3	
53190694	9.923 ± 0.004	12.529	1.00	9.3	30502	0.41	3/4	DA3+dM
952264940	1.78894 ± 0.00018	7.713	1.00	8.6	25692	1.151	1/2	DBH
219769847	8.72 ± 0.13	13.789	1.00	20.7	21620	0.72	1/1	DA3+dM
292114384	0.29255 ± 0.00014	4.110	1.00	5.1	18943	0.57	1/1	
66714896	12.579 ± 0.009	10.848	1.00	8.8	63073	0.69	1/3	
349233389	52.0 ± 5.0	31.595	1.00	25.7	23690	0.58	1/1	DA2+M
335501964	6.7654 ± 0.0025	5.380	1.00	8.1	90000	0.53	1/2	
165916724	$0.092325 \pm 5\text{e-}07$	4.156	1.00	5.2	9557	0.883	1/3	DAH
274039489	7.32 ± 0.09	67.842	1.00	58.5	42370	0.66	1/1	DA1.2+pair
328029653	14.157 ± 0.004	19.335	0.99	12.5	6340	0.53	5/5	
311920919	$0.1614889 \pm 1\text{e-}06$	4.611	1.00	6.2	14116	0.68	1/4	
155871645	$0.1385659 \pm 8\text{e-}07$	6.552	1.00	5.5	34050	0.77	3/5	
344927121	2.53418 ± 0.00018	113.339	1.00	67.3	26088	0.381	4/4	
148719841	8.549 ± 0.004	17.920	1.00	18.7	6169	0.72	2/2	
397535923	$0.206167 \pm 1.6\text{e-}05$	4.293	1.00	5.2	5222	0.537	1/2	
415714190	$0.384926 \pm 4\text{e-}06$	9.333	1.00	8.4	7690	0.636	3/3	
277713491	8.9986 ± 0.0032	11.795	1.00	9.2	7518	0.578	3/4	
471013515	6.05 ± 0.07	27.262	1.00	34.8	55000	0.6	1/1	
5393020	1.5786 ± 0.00014	54.426	1.00	49.4	8000	0.35	1/2	
610754879	$0.91146 \pm 9\text{e-}05$	11.175	1.00	10.9	47617	1.341	2/3	
365207316	2.539 ± 0.005	6.316	1.00	7.1	10520	0.226	2/2	
425079955	17.076 ± 0.016	20.821	1.00	16.2	14252	0.285	2/2	
1271382181	7.426 ± 0.005	40.083	1.00	21.8	24015	0.25	8/8	
115970839	2.6994 ± 0.0004	41.932	1.00	30.0	8825	0.219	5/5	DA+M:
159819681	10.728 ± 0.006	29.967	1.00	22.8	27876	0.573	5/5	
158971558	6.327 ± 0.004	7.300	1.00	7.3	14319	0.323	2/2	
1550807820	$0.566897 \pm 1.6\text{e-}05$	5.636	1.00	8.6	44523	1.293	5/5	
7622101	8.5708 ± 0.0028	11.742	1.00	7.6	14159	0.2	7/7	
349993999	4.381 ± 0.0005	7.642	1.00	7.0	24751	0.756	1/1	

TIC	Period [h]	Amplitude [σ]	Like	\langle Height [σ]	T_{eff} [K]	Mass [M_{\odot}]		info
1688534307	$0.0902002 \pm 4\text{e-}07$	4.253	1.00	5.3	66522	0.637	1/2	
62918265	4.6612 ± 0.0008	12.845	0.99	13.1	8133	0.724	6/6	
1922433415	2.03387 ± 0.00015	129.416	1.00	60.4	21155	0.214	2/2	
100469915	12.936 ± 0.006	18.310	1.00	21.6	12644	0.152	2/2	
2026050241	8.0844 ± 0.0024	6.393	1.00	5.7	48831	0.489	1/2	
60112260	7.37 ± 0.1	14.436	1.00	20.0	7682	0.756	1/1	
269937578	7.2969 ± 0.0019	79.671	1.00	45.4	32755	0.274	4/5	
2052430471	$0.125404 \pm 2.9\text{e-}05$	4.277	1.00	5.4	28678	0.368	1/1	
124573902	7.9918 ± 0.0035	21.546	1.00	21.9	12173	0.371	2/2	eclipse
270432557	9.311 ± 0.01	6.316	1.00	5.4	10000	0.23	2/3	
43529091	9.44 ± 0.14	11.479	1.00	14.0	11006	0.17	1/1	
278861557	3.1624 ± 0.0004	26.520	1.00	7.8	10460	0.23	19/20	pair
62846288	$0.500906 \pm 1.4\text{e-}05$	23.831	1.00	17.9	16268	0.935	3/4	
56813164	8.05 ± 0.11	25.988	1.00	34.7	17304	0.39	1/1	DA+M
953086708	$0.088138 \pm 1.3\text{e-}05$	5.293	1.00	7.4	7735	0.564	1/1	DAEH
95475692	1.94319 ± 0.00021	45.117	1.00	36.2	13737	0.428	2/2	DA+M
68015843	3.015 ± 0.0018	21.609	1.00	21.7	12392	0.4	2/2	DA+M4.5
219485299	1.9770 ± 0.0020	4.513	1.00	18.9	10307	0.63	3/3	DA+M
1507548590	1.9272 ± 0.0004	50.124	1.00	49.2	25089	0.214	2/2	
1101327387	$1.30545 \pm 9\text{e-}05$	21.739	1.00	19.5	15659	1.13	2/2	DAH
416538823	16.021 ± 0.011	335.044	1.00	26.1	18840	0.8	4/4	DA+M
7983187	14.32 ± 0.16	77.693	1.00	45.2	17210	0.59	2/2	DA3+dM
251857373	2.31675 ± 0.00012	175.807	1.00	110.6	40698	0.56	2/2	
408015814	29.52 ± 0.05	13.089	1.00	11.8	76010	0.061	2/2	
200725303	9.48 ± 0.07	35.024	1.00	33.5	90000	0.75	2/2	
159894126	0.46415 ± 0.00017	4.410	1.00	5.9	8627	0.613	1/2	
651923454	42.4 ± 2.9	16.656	1.00	11.9	21644	0.746	1/1	pair
651337335	30.5 ± 1.5	6.331	1.00	9.7	21796	0.217	1/1	
650999219	24.6 ± 0.5	24.641	1.00	26.3	70000	0.49	2/2	
93031595	9.94 ± 0.16	17.306	1.00	25.7	8751	0.911	1/1	DZ
685012668	2.8735 ± 0.0018	107.688	1.00	44.9	20041	0.238	5/5	
672383331	17.8 ± 0.5	7.107	1.00	10.9	21076	0.279	1/1	
257689590	13.35 ± 0.13	5.132	0.99	5.2	8629	0.183	2/2	
455072135	11.36 ± 0.21	90.850	1.00	49.0	12965	0.116	1/1	EB
941411508	10.547 ± 0.006	8.630	1.00	9.1	40000	0.556	2/2	
942842236	8.233 ± 0.004	10.210	1.00	10.1	77164	0.75	2/2	
332828037	2.07518 ± 0.00024	15.973	1.00	17.4	13936	0.382	2/2	
939953390	29.85 ± 0.05	9.949	1.00	6.7	63208	0.667	3/3	
952000432	21.158 ± 0.025	23.145	1.00	23.4	81500	0.58	2/2	
232524621	3.4918 ± 0.0005	14.341	1.00	8.5	100000	0.65	2/9	hotDA+pair
1003414425	26.46 ± 0.04	25.074	1.00	16.5	18089	0.173	4/4	
233177285	15.194 ± 0.01	4.790	1.00	6.2	6500	0.2	2/6	
232979174	8.8045 ± 0.0033	8.642	1.00	5.6	12776	0.473	2/9	
1001602651	4.9125 ± 0.0018	10.704	1.00	7.2	9786	0.826	5/6	
219009693	1.5828 ± 0.0004	9.973	1.00	7.3	14000	0.23	4/4	
364160098	$0.19744 \pm 6\text{e-}05$	4.307	1.00	5.7	20000	0.2	1/1	
471013541	0.549 ± 0.0005	4.071	1.00	5.6	88642	0.51	1/1	
951282189	2.9618 ± 0.0005	95.469	0.99	110.8	19099	0.174	2/2	DAB+pair

TIC	Period [h]	Amplitude [σ]	Like	\langle Height [σ]	T_{eff} [K]	Mass [M_{\odot}]		info
951635495	23.45 \pm 0.03	7.002	1.00	6.6	61045	0.5	2/2	
1924161836	25.132 \pm 0.024	14.278	1.00	12.4	71080	0.482	2/2	
410414842	14.9 \pm 0.4	6.417	1.00	9.7	70000	0.5	1/1	
2052284133	16.652 \pm 0.03	12.980	1.00	14.3	34299	0.51	2/2	
251080865	32.01 \pm 0.06	179.265	1.00	38.0	7170	0.744	2/2	DCP7
164681986	3.9437 \pm 0.0009	33.642	1.00	31.3	8471	1.006	2/2	
392797216	0.6808 \pm 0.0004	6.037	1.00	6.0	6814	0.749	2/2	DAH
157201137	0.776229 \pm 3.3e-05	10.198	1.00	10.9	11254	0.486	2/2	CV
219868627	5.9071 \pm 0.0017	43.787	1.00	18.3	18000	0.18	12/12	DAZ+pair
155872634	3.9145 \pm 0.0007	26.280	1.00	16.7	24589	0.697	6/6	
357389336	42.46 \pm 0.08	7.007	1.00	6.1	21785	0.49	2/5	DA+K
313894558	19.05 \pm 0.04	4.861	0.99	5.2	18610	0.61	1/2	
441569276	2.47353 \pm 0.00023	90.759	1.00	55.4	19690	0.43	6/6	DA+M
457099062	1.36615 \pm 0.0002	7.658	1.00	8.2	6655	0.555	2/2	
198510602	8.87 \pm 0.013	110.918	1.00	46.3	9800	0.23	4/4	
236865474	17.789 \pm 0.011	55.795	1.00	21.0	26520	0.52	14/14	DA1.9+pair
279484490	0.086195 \pm 1.2e-05	4.519	1.00	5.8	16989	0.387	1/1	
248353420	11.32 \pm 0.26	105.385	1.00	69.0	60419	0.53	1/1	DA+K
54003343	22.864 \pm 0.029	16.612	1.00	18.5	52869	0.611	1/2	DA1+dM
71513592	23.0 \pm 0.9	11.500	1.00	15.8	39910	0.438	1/1	
737660462	9.703 \pm 0.013	30.331	1.00	23.7	30415	0.502	5/5	
60040774	9.72 \pm 0.15	9.104	1.00	14.7	8876	0.277	1/1	eclipse
712210226	0.115822 \pm 2.2e-05	4.178	1.00	5.5	13707	0.53	1/1	pair
705867935	0.28689 \pm 0.00013	6.605	1.00	13.7	16407	1.001	1/1	
765410943	3.7702 \pm 0.0005	169.012	1.00	55.6	22601	0.238	19/19	
96391732	3.662 \pm 0.011	98.438	1.00	117.0	21272	0.183	2/2	
291303146	14.36 \pm 0.33	43.492	1.00	40.9	100000	0.58	1/1	
770913638	0.453289 \pm 1.1e-05	19.139	1.00	21.2	8474	0.794	2/2	
743328948	7.9 \pm 0.1	28.663	1.00	45.6	20000	0.2	1/1	
403672198	3.137 \pm 0.016	25.892	1.00	38.6	7750	0.23	1/1	
437213912	37.1 \pm 2.3	29.331	1.00	34.2	9000	0.2	1/1	
836046041	7.9019 \pm 0.0034	12.734	1.00	15.5	26187	0.517	2/2	
817911025	0.597463 \pm 1.9e-05	17.981	1.00	16.0	84000	0.63	3/4	
832516183	30.55 \pm 0.05	9.190	1.00	9.2	28583	0.403	1/1	
804549027	2.948 \pm 0.007	117.121	1.00	79.0	10000	0.2	2/2	
191532802	3.553 \pm 0.022	5.513	1.00	11.6	8630	0.808	1/1	
262708252	5.4411 \pm 0.0015	28.747	1.00	16.1	10266	0.152	7/7	
841325183	2.504 \pm 0.0005	10.370	1.00	9.2	17205	0.28	3/4	
873285117	20.79 \pm 0.024	9.782	1.00	9.9	37453	0.349	1/2	
875311151	11.053 \pm 0.007	9.792	1.00	8.7	50475	0.491	1/2	
309025727	8.22 \pm 0.06	19.948	1.00	26.6	9000	0.23	1/2	
870310469	23.443 \pm 0.03	9.701	1.00	9.9	37491	0.502	2/2	
841399917	36.32 \pm 0.15	64.304	1.00	39.3	17000	0.2	4/4	
33357141	13.47 \pm 0.31	8.387	1.00	11.5	24952	0.526	1/1	
345036441	1.64579 \pm 8e-05	13.629	1.00	10.6	10355	0.92	4/5	DAH
471013677	2.79285 \pm 0.00031	59.858	1.00	53.6	36470	0.6	1/4	
902670676	22.988 \pm 0.029	10.934	1.00	10.8	78000	0.66	2/2	
82347011	6.2108 \pm 0.0021	130.009	1.00	94.0	30071	0.4	2/2	DA+M3

TIC	Period [h]	Amplitude [σ]	Like	\langle Height [σ]	T_{eff} [K]	Mass [M_{\odot}]		info
950218375	10.3 ± 0.19	7.101	1.00	10.0	42180	0.52	1/1	
232972481	81.13 ± 0.28	89.769	1.00	39.0	99575	0.87	7/7	DA+M
156073827	$0.189861 \pm 2\text{e-}06$	10.486	1.00	10.0	29300	0.415	2/3	
115613388	$0.703919 \pm 2.6\text{e-}05$	6.117	1.00	5.3	28169	1.272	2/5	DAH
630123582	4.109 ± 0.027	3.846	1.00	12.5	60000	0.456	1/1	
630314437	$0.17219 \pm 5\text{e-}05$	4.425	1.00	6.9	21128	0.526	1/1	pair
399570361	10.89 ± 0.22	25.327	0.99	27.6	79000	0.656	1/1	pair
183799565	$0.689793 \pm 2.6\text{e-}05$	5.825	1.00	5.8	180000	0.54	1/4	
142982488	0.40188 ± 0.00026	4.112	1.00	5.6	34180	0.626	1/1	
298411553	2.90014 ± 0.00031	12.166	1.00	8.2	39229	0.756	4/8	
80858168	2.84122 ± 0.0003	38.679	1.00	34.0	12891	0.256	3/3	
652008669	48.0 ± 4.0	6.901	1.00	6.0	31092	0.432	1/1	
412252434	2.40744 ± 0.00022	7.758	1.00	12.8	10206	0.597	4/4	
760481896	6.641 ± 0.005	64.546	1.00	32.8	27691	0.404	4/4	
453006983	9.093 ± 0.005	19.789	1.00	21.5	27425	0.52	2/2	DA+M
804378446	29.44 ± 0.05	12.366	1.00	14.6	48986	0.685	2/2	
310478036	2.36875 ± 0.00029	11.001	1.00	59.3	7000	0.23	7/7	
349408306	3.6493 ± 0.0005	84.357	1.00	25.5	8000	0.15	21/21	
462519068	4.987 ± 0.008	4.490	1.00	19.7	7000	0.15	3/3	
119736060	3.954 ± 0.026	49.116	1.00	56.6	22600	0.42	1/1	DA+M
46199750	1.891 ± 0.008	7.440	1.00	13.9	20000	0.94	1/1	DAP
147918835	2.722 ± 0.012	156.826	1.00	63.5	24661	0.21	1/1	
142808656	7.9038 ± 0.0034	11.463	1.00	10.0	18646	0.031	4/4	
258086867	30.3 ± 1.5	7.607	1.00	5.6	7573	0.753	1/1	
1000946479	2.69774 ± 0.00032	4.572	1.00	5.8	7139	0.6	1/4	DC
274928438	2.464 ± 0.01	5.552	1.00	6.6	6959	0.23	1/1	DA+M
1100582330	2.736 ± 0.017	18.131	1.00	29.2	26828	0.496	1/1	
284900652	7.9923 ± 0.0021	359.311	1.00	71.7	34733	0.36	29/29	DA+dMe
383673264	72.37 ± 0.17	15.671	1.00	6.8	11435	0.661	11/25	
25771075	7.8738 ± 0.0023	14.170	1.00	14.5	15849	0.263	3/3	
47499442	7.83 ± 0.1	18.473	1.00	22.7	7184	0.562	1/1	
33692053	15.1 ± 0.4	14.656	1.00	20.4	24809	0.239	1/1	
34855316	4.461 ± 0.032	30.907	1.00	46.5	8021	0.745	1/1	
355154138	2.37013 ± 0.00029	18.259	1.00	11.4	14569	0.403	7/7	
429233827	7.17 ± 0.0028	113.682	1.00	74.9	10618	0.174	2/2	
32159409	42.8 ± 3.2	9.008	1.00	11.7	10000	0.2	1/1	
1550940367	21.89 ± 0.19	21.620	1.00	15.7	50000	0.425	4/4	
91193988	3.6933 ± 0.0005	18.393	1.00	19.9	13597	0.249	2/2	
192991819	1.81005 ± 0.00018	34.905	1.00	35.9	7000	0.23	3/3	double-eclipse
73764818	$0.135393 \pm 3.2\text{e-}05$	4.101	1.00	5.0	35994	0.464	1/1	
178539314	4.3923 ± 0.0011	5.228	1.00	7.8	8201	0.422	2/2	
938779482	0.4613 ± 0.0004	8.293	0.96	14.2	10000	0.2	1/1	double-eclipse
251903434	34.6 ± 1.9	109.202	0.98	28.1	7752	0.702	1/1	
159394587	14.753 ± 0.021	7.390	0.85	5.2	16890	0.6	1/4	
74342209	1.557 ± 0.004	146.008	0.87	44.0	9463	0.478	1/1	
1201364356	276.0 ± 6.0	483.909	0.86	20.9	12816	0.61	11/15	pair-disk?
398365709	8.0828 ± 0.0018	72.725	0.92	19.0	22570	0.54	5/5	DA+M
245830829	13.56 ± 0.15	300.596	0.96	18.7	17620	0.63	2/2	DA3+M

TIC	Period [h]	Amplitude [σ]	Like	\langle Height [σ]	T_{eff} [K]	Mass [M_{\odot}]		info
329670050	2.703 ± 0.011	99.642	0.98	34.9	9000	0.23	1/1	
243349100	23.447 ± 0.028	14.703	0.98	8.6	7250	0.23	5/6	
1920685932	25.12 ± 0.06	40.975	0.99	12.5	11981	0.388	1/2	pair
269663822	4.5085 ± 0.0008	226.862	0.98	75.2	7000	0.2	20/20	
403292348	3.3522 ± 0.0012	280.702	0.98	101.4	8000	0.2	2/2	
15131739	6.143 ± 0.004	17.562	0.99	16.5	31194	0.403	2/2	DA+L3
142616553	181.0 ± 1.7	31.440	0.84	19.0	14635	0.48	4/6	pair
901406326	$0.113414 \pm 2.2\text{e-}05$	5.396	0.87	9.5	114711	0.701	1/1	
115013365	1.20234 ± 0.00005	6.454	1.00	9.0	12826	0.23	1/2	
269071459	21.51 ± 0.025	17.219	0.98	10.5	9375	0.852	5/5	
137607346	23.927 ± 0.025	190.904	0.98	58.7	9000	0.2	6/6	
458692929	27.4 ± 1.2	5.070	0.84	8.2	35105	0.36	1/1	DA+pair
311948770	16.932 ± 0.01	219.451	0.80	89.7	49650	0.66	5/5	DAO+M
903362877	65.4 ± 1.3	14.507	0.98	5.2	18344	0.488	1/3	pair
158747696	2.041 ± 0.007	23.570	0.98	27.8	8000	0.205	1/1	pair
8158475	56.85 ± 0.18	8.819	0.99	6.9	45333	0.527	1/2	
1990690286	15.322 ± 0.009	17.081	1.00	16.1	100000	0.48	2/2	
814547613	3.3579 ± 0.0006	27.264	0.96	19.8	14115	0.567	2/4	
88509155	128.0 ± 27.0	28.056	1.00	29.4	56610	0.53	1/1	DA+M
1951569775	92.9 ± 0.9	237.305	1.00	36.3	7000	0.2	2/2	
115075496	53.0 ± 4.0	9.833	1.00	9.9	44715	0.469	1/1	DA+M:
118690168	34.85 ± 0.07	7.436	1.00	6.2	11023	0.587	2/3	
138653638	213.5 ± 2.6	40.343	0.78	17.0	12436	0.478	3/4	pair
721486224	150.0 ± 50.0	150.795	0.84	17.1	11692	0.725	3/3	pair
1101853877	121.0 ± 11.0	102.164	1.00	7.0	18791	0.673	1/2	DA+pair
453444667	82.1 ± 1.5	111.345	1.00	59.4	105000	0.75	2/2	DA+BP
246847488	173.0 ± 5.0	51.455	1.00	21.5	5720	0.1	1/1	
262548040	$2^* (0.10614391 \pm 0.00000025)$	6.409	1.00	6.2	6230	0.41	3/5	DA7H
229098638	181.6 ± 0.7	815.491	1.00	19.2	18800	0.56	4/4	pair
404156391	28.133 ± 0.030	221.896	0.97	8.8	17770	0.542	2/2	pair
204440456	6.20 ± 0.07	18.679	1.00	21.3	6908	0.6018	1/1	
732235000	23.667 ± 0.020	19.728	1.00	8.5	19212	0.523	11/16	pair
50385872	5.4166 ± 0.0007	5.535	1.00	5.6	13141	0.710	2/8	
61965938	6.8168 ± 0.0013	51.961	1.00	5.1	19505	0.633	1/3	
1174761001	5.7114 ± 0.0018	23.495	1.00	24.2	18311	0.511	2/2	pair
23936802	5.8054 ± 0.0018	17.076	1.00	27.0	17146	0.269	4/4	
253936074	45.16 ± 0.07	25.890	1.00	5.5	0.676	pair	1/2	
2055541164	2.53003 ± 0.00023	73.753	1.00	48.6	23575	0.261	4/4	
408253347	7.9829 ± 0.0034	49.765	1.00	36.4	24466	0.47	2/3	DA+dMe
611305959	21.84 ± 0.05	21.142	1.00	16.4	90000	0.6	3/3	
611853501	0.385874 ± 0.000006	13.347	1.00	14.9	21697	1.055	2/2	
2024143938	1.1367 ± 0.0023	17.506	1.00	29.1	20000	0.323	1/1	DAZ+L3
380174982	4.4379 ± 0.0005	15.711	0.98	15.3	8607	0.83	3/3	
219099282	77.17 ± 0.20	22.276	1.00	6.3	45230	0.63	15/25	
610721330	0.671865 ± 0.000017	5.779	1.00	5.0	24332	1.218	1/4	
161820334	6.9232 ± 0.002	32.422	1.00	15.3	18462	0.183	6/7	
441702898	8.3222 ± 0.0029	13.601	0.99	8.6	7501	0.445	6/6	
144197100	0.245758 ± 0.000008	16.037	1.00	16.5	8595	0.87	2/2	

TIC	Period [h]	Amplitude [σ]	Like	\langle Height [σ]	T_{eff} [K]	Mass [M_{\odot}]		info
841424790	3.311 ± 0.0004	7.040	1.00	6.0	73027	0.751	3/7	

REFERENCES

- 2014, Society of Photo-Optical Instrumentation Engineers (SPIE) Conference Series, Vol. 9143, Space Telescopes and Instrumentation 2014: Optical, Infrared, and Millimeter Wave
- Adams, W. S. 1915, *PASP*, 27, 236, doi: [10.1086/122440](https://doi.org/10.1086/122440)
- Aerts, C., & Tkachenko, A. 2023, arXiv e-prints, arXiv:2311.08453, doi: [10.48550/arXiv.2311.08453](https://doi.org/10.48550/arXiv.2311.08453)
- Amorim, L. L., Kepler, S. O., Külebi, B., Jordan, S., & Romero, A. D. 2023, *ApJ*, 944, 56, doi: [10.3847/1538-4357/acaf6e](https://doi.org/10.3847/1538-4357/acaf6e)
- Barstow, M. A., Jordan, S., O'Donoghue, D., et al. 1995, *MNRAS*, 277, 971, doi: [10.1093/mnras/277.3.971](https://doi.org/10.1093/mnras/277.3.971)
- Bell, K. J. 2020, in American Astronomical Society Meeting Abstracts, Vol. 235, American Astronomical Society Meeting Abstracts #235, 106.06
- Bell, K. J., Hermes, J. J., Vanderbosch, Z., et al. 2017, *The Astrophysical Journal*, 851, 24, doi: [10.3847/1538-4357/aa9702](https://doi.org/10.3847/1538-4357/aa9702)
- Bloeker, T. 1995, *A&A*, 297, 727
- Böhm-Vitense, E. 1958, *Zeitschrift für Astrophysik*, 46, 108
- Bond, H. E., Kawaler, S. D., Ciardullo, R., et al. 1996, *AJ*, 112, 2699, doi: [10.1086/118214](https://doi.org/10.1086/118214)
- Bradley, P. A. 2001, *The Astrophysical Journal*, 552, 326, doi: [10.1086/320454](https://doi.org/10.1086/320454)
- Brinkworth, C. S., Burleigh, M. R., Lawrie, K., Marsh, T. R., & Knigge, C. 2013, *The Astrophysical Journal*, 773, 47, doi: [10.1088/0004-637X/773/1/47](https://doi.org/10.1088/0004-637X/773/1/47)
- Caiazzo, I., Burdge, K. B., Fuller, J., et al. 2021, *Nature*, 595, 39, doi: [10.1038/s41586-021-03615-y](https://doi.org/10.1038/s41586-021-03615-y)
- Calcaferro, Leila M., Córscico, Alejandro H., & Althaus, Leandro G. 2016, *A&A*, 589, A40, doi: [10.1051/0004-6361/201527996](https://doi.org/10.1051/0004-6361/201527996)
- Caldwell, D. A., Tenenbaum, P., Twicken, J. D., et al. 2020, *Research Notes of the American Astronomical Society*, 4, 201, doi: [10.3847/2515-5172/abc9b3](https://doi.org/10.3847/2515-5172/abc9b3)
- Castanheira, B. G., Kepler, S. O., Kleinman, S. J., Nitta, A., & Fraga, L. 2013, *MNRAS*, 430, 50, doi: [10.1093/mnras/sts474](https://doi.org/10.1093/mnras/sts474)
- Catalán, S., Isern, J., García-Berro, E., & Ribas, I. 2008, *MNRAS*, 387, 1693, doi: [10.1111/j.1365-2966.2008.13356.x](https://doi.org/10.1111/j.1365-2966.2008.13356.x)
- Choi, J., Dotter, A., Conroy, C., et al. 2016, *ApJ*, 823, 102, doi: [10.3847/0004-637X/823/2/102](https://doi.org/10.3847/0004-637X/823/2/102)
- Córscico, A. H., Uzundag, M., Kepler, S. O., et al. 2021, *A&A*, 645, A117, doi: [10.1051/0004-6361/202039202](https://doi.org/10.1051/0004-6361/202039202)
- Diaz-Pinto, A., Garcia-Berro, E., Hernanz, M., Isern, J., & Mochkovitch, R. 1994, *A&A*, 282, 86
- Doherty, C. L., Gil-Pons, P., Siess, L., Lattanzio, J. C., & Lau, H. H. B. 2014, *Monthly Notices of the Royal Astronomical Society*, 446, 2599, doi: [10.1093/mnras/stu2180](https://doi.org/10.1093/mnras/stu2180)
- Dolez, N., Vauclair, G., Kleinman, S. J., et al. 2006, *A&A*, 446, 237, doi: [10.1051/0004-6361:20053149](https://doi.org/10.1051/0004-6361:20053149)
- Dominguez, I., Chieffi, A., Limongi, M., & Straniero, O. 1999, *ApJ*, 524, 226, doi: [10.1086/307787](https://doi.org/10.1086/307787)
- Farihi, J., Robert, A., & Walters, N. 2023, A Nearby Polluted White Dwarf with a 6.2 h Spin Period. <https://arxiv.org/abs/2312.03845>
- Fritzewski, D. J., Barnes, S. A., James, D. J., & Strassmeier, K. G. 2021, *A&A*, 652, A60, doi: [10.1051/0004-6361/202140894](https://doi.org/10.1051/0004-6361/202140894)
- Fu, J.-N., Dolez, N., Vauclair, G., et al. 2012, *Monthly Notices of the Royal Astronomical Society*, 429, 1585, doi: [10.1093/mnras/sts438](https://doi.org/10.1093/mnras/sts438)
- Fu, J.-N., Vauclair, G., Su, J., et al. 2019, *Monthly Notices of the Royal Astronomical Society*, 486, 3560, doi: [10.1093/mnras/stz1088](https://doi.org/10.1093/mnras/stz1088)
- Fu, J.-N., Vauclair, G., Solheim, J.-E., et al. 2007, *A&A*, 467, 237, doi: [10.1051/0004-6361:20066295](https://doi.org/10.1051/0004-6361:20066295)
- Gaia Collaboration, Babusiaux, C., van Leeuwen, F., et al. 2018, *A&A*, 616, A10, doi: [10.1051/0004-6361/201832843](https://doi.org/10.1051/0004-6361/201832843)
- García-Berro, E., Isern, J., & Hernanz, M. 1997, *Monthly Notices of the Royal Astronomical Society*, 289, 973, doi: [10.1093/mnras/289.4.973](https://doi.org/10.1093/mnras/289.4.973)
- Gentile Fusillo, N. P., Tremblay, P. E., Cukanovaite, E., et al. 2021, *MNRAS*, 508, 3877, doi: [10.1093/mnras/stab2672](https://doi.org/10.1093/mnras/stab2672)
- Giammichele, N., Fontaine, G., Brassard, P., & Charpinet, S. 2016, *The Astrophysical Journal Supplement Series*, 223, 10, doi: [10.3847/0067-0049/223/1/10](https://doi.org/10.3847/0067-0049/223/1/10)
- Greiss, S., Gänsicke, B. T., Hermes, J. J., et al. 2014, *Monthly Notices of the Royal Astronomical Society*, 438, 3086, doi: [10.1093/mnras/stt2420](https://doi.org/10.1093/mnras/stt2420)
- Guo, J., Zhao, J., Zhang, H., et al. 2022, *MNRAS*, 509, 2674, doi: [10.1093/mnras/stab3151](https://doi.org/10.1093/mnras/stab3151)

- 843 Heger, A., Langer, N., & Woosley, S. E. 2000, *ApJ*, 528,
844 368, doi: [10.1086/308158](https://doi.org/10.1086/308158)
- 845 Heger, A., Woosley, S. E., & Spruit, H. C. 2005, *ApJ*, 626,
846 350, doi: [10.1086/429868](https://doi.org/10.1086/429868)
- 847 Henyey, L., Vardya, M. S., & Bodenheimer, P. 1965, *ApJ*,
848 142, 841, doi: [10.1086/148357](https://doi.org/10.1086/148357)
- 849 Hermes, J. J., Kawaler, S. D., Bischoff-Kim, A., et al.
850 2017a, *The Astrophysical Journal*, 835, 277,
851 doi: [10.3847/1538-4357/835/2/277](https://doi.org/10.3847/1538-4357/835/2/277)
- 852 Hermes, J. J., Brown, W. R., Kilic, M., et al. 2014, *ApJ*,
853 792, 39, doi: [10.1088/0004-637X/792/1/39](https://doi.org/10.1088/0004-637X/792/1/39)
- 854 Hermes, J. J., Gänsicke, B. T., Kawaler, S. D., et al. 2017b,
855 *ApJS*, 232, 23, doi: [10.3847/1538-4365/aa8bb5](https://doi.org/10.3847/1538-4365/aa8bb5)
- 856 Higgins, M. E., & Bell, K. J. 2023, *AJ*, 165, 141,
857 doi: [10.3847/1538-3881/acb20c](https://doi.org/10.3847/1538-3881/acb20c)
- 858 Höfner, S., & Olofsson, H. 2018, *A&A Rv*, 26, 1,
859 doi: [10.1007/s00159-017-0106-5](https://doi.org/10.1007/s00159-017-0106-5)
- 860 Jermyn, A. S., Bauer, E. B., Schwab, J., et al. 2023, *ApJS*,
861 265, 15, doi: [10.3847/1538-4365/aca8d](https://doi.org/10.3847/1538-4365/aca8d)
- 862 Kawaler, S. D. 2015, in *Astronomical Society of the Pacific*
863 *Conference Series*, Vol. 493, 19th European Workshop on
864 *White Dwarfs*, ed. P. Dufour, P. Bergeron, &
865 G. Fontaine, 65, doi: [10.48550/arXiv.1410.6934](https://doi.org/10.48550/arXiv.1410.6934)
- 866 Kawaler, S. D., O'Brien, M. S., Clemens, J. C., et al. 1995,
867 *ApJ*, 450, 350, doi: [10.1086/176145](https://doi.org/10.1086/176145)
- 868 Kepler, S., & Romero, A. D. 2017, *EPJ Web Conf.*, 152,
869 01011, doi: [10.1051/epjconf/201715201011](https://doi.org/10.1051/epjconf/201715201011)
- 870 Kepler, S. O. 1993, *Baltic Astronomy*, 2, 515,
871 doi: [10.1515/astro-1993-3-425](https://doi.org/10.1515/astro-1993-3-425)
- 872 Kepler, S. O., Koester, D., Pelisoli, I., Romero, A. D., &
873 Ourique, G. 2021, *Monthly Notices of the Royal*
874 *Astronomical Society*, 507, 4646,
875 doi: [10.1093/mnras/stab2411](https://doi.org/10.1093/mnras/stab2411)
- 876 Kepler, S. O., Koester, D., Pelisoli, I., Romero, A. D., &
877 Ourique, G. 2021, *MNRAS*, 507, 4646,
878 doi: [10.1093/mnras/stab2411](https://doi.org/10.1093/mnras/stab2411)
- 879 Kepler, S. O., Giovannini, O., Wood, M. A., et al. 1995,
880 *ApJ*, 447, 874, doi: [10.1086/175924](https://doi.org/10.1086/175924)
- 881 Kilic, M., Bergeron, P., Kosakowski, A., et al. 2020, *ApJ*,
882 898, 84, doi: [10.3847/1538-4357/ab9b8d](https://doi.org/10.3847/1538-4357/ab9b8d)
- 883 Kilic, M., Stanek, K. Z., & Pinsonneault, M. H. 2007, *ApJ*,
884 671, 761, doi: [10.1086/522228](https://doi.org/10.1086/522228)
- 885 Kr̩t̩čka, J., Kawka, A., Mikulášek, Z., et al. 2023,
886 *Astronomy & Astrophysics*, 674, A94,
887 doi: [10.1051/0004-6361/202245551](https://doi.org/10.1051/0004-6361/202245551)
- 888 Labadie-Bartz, J., Hümmerich, S., Bernhard, K., Paunzen,
889 E., & Shultz, M. E. 2023, *A&A*, 676, A55,
890 doi: [10.1051/0004-6361/202346657](https://doi.org/10.1051/0004-6361/202346657)
- 891 Langer, N. 2012, *Annual Review of Astronomy and*
892 *Astrophysics*, 50, 107,
893 doi: [10.1146/annurev-astro-081811-125534](https://doi.org/10.1146/annurev-astro-081811-125534)
- 894 Li, C., Fu, J., Fox-Machado, L., Su, J., & Chen, F. 2017,
895 *NewA*, 55, 48, doi: [10.1016/j.newast.2017.03.003](https://doi.org/10.1016/j.newast.2017.03.003)
- 896 Lightkurve Collaboration, Cardoso, J. V. d. M., Hedges, C.,
897 et al. 2018, *Lightkurve: Kepler and TESS time series*
898 *analysis in Python*. <http://ascl.net/1812.013>
- 899 Marsh, T. R., Dhillon, V. S., & Duck, S. R. 1995, *MNRAS*,
900 275, 828, doi: [10.1093/mnras/275.3.828](https://doi.org/10.1093/mnras/275.3.828)
- 901 McCook, G. P., & Sion, E. M. 2016, *VizieR Online Data*
902 *Catalog*, 1, 2035
- 903 Moss, A., Kilic, M., Bergeron, P., Fergard, M., & Brown, W.
904 2023, *MNRAS*, 523, 5598, doi: [10.1093/mnras/stad1835](https://doi.org/10.1093/mnras/stad1835)
- 905 Mosser, B., Goupil, M. J., Belkacem, K., et al. 2012, *A&A*,
906 548, A10, doi: [10.1051/0004-6361/201220106](https://doi.org/10.1051/0004-6361/201220106)
- 907 Moyano, F. D., Eggenberger, P., Meynet, G., et al. 2022,
908 *A&A*, 663, A180, doi: [10.1051/0004-6361/202243389](https://doi.org/10.1051/0004-6361/202243389)
- 909 Moyano, F. D., Eggenberger, P., Salmon, S. J. A. J.,
910 Mombarg, J. S. G., & Ekström, S. 2023, *A&A*, 677, A6,
911 doi: [10.1051/0004-6361/202346548](https://doi.org/10.1051/0004-6361/202346548)
- 912 Nather, R. E., Winget, D. E., Clemens, J. C., Hansen, C. J.,
913 & Hine, B. P. 1990, *ApJ*, 361, 309, doi: [10.1086/169196](https://doi.org/10.1086/169196)
- 914 O'Brien, M. W., Tremblay, P. E., Gentile Fusillo, N. P.,
915 et al. 2023, *MNRAS*, 518, 3055,
916 doi: [10.1093/mnras/stac3303](https://doi.org/10.1093/mnras/stac3303)
- 917 Oliveira da Rosa, G., Kepler, S. O., Córscico, A. H., et al.
918 2022, *ApJ*, 936, 187, doi: [10.3847/1538-4357/ac8871](https://doi.org/10.3847/1538-4357/ac8871)
- 919 Østensen, R. H., Bloemen, S., Vučković, M., et al. 2011,
920 *ApJL*, 736, L39, doi: [10.1088/2041-8205/736/2/L39](https://doi.org/10.1088/2041-8205/736/2/L39)
- 921 Paxton, B., Bildsten, L., Dotter, A., et al. 2011, *ApJS*, 192,
922 3, doi: [10.1088/0067-0049/192/1/3](https://doi.org/10.1088/0067-0049/192/1/3)
- 923 Paxton, B., Cantiello, M., Arras, P., et al. 2013, *ApJS*, 208,
924 4, doi: [10.1088/0067-0049/208/1/4](https://doi.org/10.1088/0067-0049/208/1/4)
- 925 Paxton, B., Marchant, P., Schwab, J., et al. 2015, *ApJS*,
926 220, 15, doi: [10.1088/0067-0049/220/1/15](https://doi.org/10.1088/0067-0049/220/1/15)
- 927 Paxton, B., Schwab, J., Bauer, E. B., et al. 2018, *ApJS*,
928 234, 34, doi: [10.3847/1538-4365/aaa5a8](https://doi.org/10.3847/1538-4365/aaa5a8)
- 929 Paxton, B., Smolec, R., Schwab, J., et al. 2019, *ApJS*, 243,
930 10, doi: [10.3847/1538-4365/ab2241](https://doi.org/10.3847/1538-4365/ab2241)
- 931 Pech, D., & Vauclair, G. 2006, *A&A*, 453, 219,
932 doi: [10.1051/0004-6361:20054370](https://doi.org/10.1051/0004-6361:20054370)
- 933 Pedersen, M. G., & Bell, K. J. 2023, *AJ*, 165, 239,
934 doi: [10.3847/1538-3881/accc31](https://doi.org/10.3847/1538-3881/accc31)
- 935 Pfeiffer, B., Vauclair, G., Dolez, N., et al. 1996, *A&A*, 314,
936 182
- 937 Poelarends, A. J. T., Herwig, F., Langer, N., & Heger, A.
938 2008, *The Astrophysical Journal*, 675, 614,
939 doi: [10.1086/520872](https://doi.org/10.1086/520872)

- 940 Reimers, D. 1975, *Memoires of the Societe Royale des*
941 *Sciences de Liege*, 8, 369
- 942 Rohrmann, R. D., Althaus, L. G., & Kepler, S. O. 2011,
943 *MNRAS*, 411, 781, doi: [10.1111/j.1365-2966.2010.17716.x](https://doi.org/10.1111/j.1365-2966.2010.17716.x)
- 944 Romero, A. D., Campos, F., & Kepler, S. O. 2015,
945 *MNRAS*, 450, 3708, doi: [10.1093/mnras/stv848](https://doi.org/10.1093/mnras/stv848)
- 946 Romero, A. D., Kepler, S. O., Hermes, J. J., et al. 2022,
947 *Monthly Notices of the Royal Astronomical Society*, 511,
948 1574, doi: [10.1093/mnras/stac093](https://doi.org/10.1093/mnras/stac093)
- 949 Siess, L. 2010, *A&A*, 512, A10,
950 doi: [10.1051/0004-6361/200913556](https://doi.org/10.1051/0004-6361/200913556)
- 951 Su, J., Li, Y., Fu, J.-N., & Li, C. 2013, *Monthly Notices of*
952 *the Royal Astronomical Society*, 437, 2566,
953 doi: [10.1093/mnras/stt2069](https://doi.org/10.1093/mnras/stt2069)
- 954 Tremblay, P. E., Hollands, M. A., Gentile Fusillo, N. P.,
955 et al. 2020, *MNRAS*, 497, 130,
956 doi: [10.1093/mnras/staa1892](https://doi.org/10.1093/mnras/staa1892)
- 957 Wenger, M., Ochsenbein, F., Egret, D., et al. 2000, *A&AS*,
958 143, 9, doi: [10.1051/aas:2000332](https://doi.org/10.1051/aas:2000332)
- 959 Williams, K. A., Hermes, J. J., & Vanderbosch, Z. P. 2022,
960 *AJ*, 164, 131, doi: [10.3847/1538-3881/ac8543](https://doi.org/10.3847/1538-3881/ac8543)
- 961 Woosley, S. E., & Heger, A. 2015, *The Astrophysical*
962 *Journal*, 810, 34, doi: [10.1088/0004-637X/810/1/34](https://doi.org/10.1088/0004-637X/810/1/34)
- 963 Zahn, J. P. 1977, *A&A*, 57, 383